Reflectance spectra of mascagnite and salammoniac minerals with varying viewing geometry

M. Fastelli, B. Schmitt, P. Beck, O. Poch, A. Zucchini, F. Frondini, P. Comodi

This is the Accepted Manuscript of this published paper: Fastelli, M., Schmitt, B., Beck, P., Poch, O., Zucchini, A., Frondini, F., Comodi, P., 2023. Reflectance spectra of mascagnite and salammoniac minerals with varying viewing geometry. Icarus 403, 115633. https://doi.org/10.1016/j.icarus.2023.115633

Reflectance spectra of mascagnite and salammoniac minerals with varying viewing geometry.

Fastelli M.[a*], Schmitt B.[b], Beck P.[b], Poch O.[b], Zucchini A.[a], Frondini F.[a] and Comodi P.[a]

a Department of Physics and Geology, University of Perugia, I-06123, Perugia, Italy

b Univ. Grenoble Alpes, CNRS, IPAG, 38000 Grenoble, France

*Email: maximiliano.fastelli@unipg.it

Highlights

- Mascagnite-$(NH_4)_2SO_4$ and salammoniac-NH_4Cl minerals were characterized by means of BRDF spectroscopy with varying viewing geometries in term of incidence (*i*) and emergence (*e*) angles.
- Relationship between the viewing geometry variations and the spectral feature parameters (band area, depth, slope) of NH_4^+ features were observed.
- High spectral variability was observed for $i \geq 30°$ and $e \geq 60°$ angles.
- Results from such investigation will be useful to interpret occurrence of ammonium salts on planetary surfaces, especially small bodies.

Abstract

We analyse the quantitative effects of viewing geometry variations on the near-infrared reflectance spectra of mascagnite-$(NH_4)_2SO_4$ and salammoniac-NH_4Cl samples. Bi-directional reflectance spectra are collected in the 1 - 4.2 µm range considering a set of 3 incidence (*i*) angles (*i* = 0°; 30°; 60°) and 9 emergence (*e*) angles between -70° and 70° at room temperature and computed with respect to the normal direction. The NH_4^+ overtone and combinations bands located at ~ 1.09, 1.32, 1.62, 2.04, 2.2 and 3.05 µm are experimentally investigated. The bidirectional reflectance spectra of these samples show significant variations with the observation geometry in terms of reflectance values, spectral slope, and absorption bands parameters. The band positions remain essentially unchanged by varying the incident and emergence angles. On the other hand, bands' area and depth show the highest variability for $i \geq 30°$ and *e* greater than ±40°(up to a factor 2.3 in relative mean variation). The area and depth parameters of these bands show a dual behaviour: (i) for the weak-medium spectral features below 2 µm the area and depth decrease as the phase angle increases. (ii) The strong spectral features above 2 µm increase their values only at phase angles above 90°, but also at low phase angles for high incidences, $i \geq 30°$. This behaviour is linked both to the non-linear radiative transfer in particulate media and to the way the band depth and area are defined, relative to the local continuum. We observe important dependence (up to ~60% relative mean variation) of band depth and area on the incidence angle, up to 60°, compared to moderate variation with emergence angles (up to ~20% relative mean variation). Furthermore, the ~ 3 µm features becomes more saturated at ± 70° emergence angles. A general trend of spectral bluing with change in observation geometry is observed. The current dataset is a contribution in the framework of present and future space missions focused on understanding the nature and quantification of ammonium-bearing minerals on icy bodies. The NH_4^+ – bearing minerals identification could provide

information on: (i) ocean/brine compositions, (ii) possible explanations of geological phenomena and (iii) implications for biological activity.

Keywords: mascagnite, salammoniac, reflectance spectra, icy bodies, viewing geometry.

1 Introduction

Planetary surface remote sensing by visible and near-infrared reflectance spectroscopy (0.4 -5 µm), from telescopic observations and spacecrafts, is a widely applied technique for investigating and deciphering their composition. One way to resolve and identify which are the best candidates to represent surface compositions of planetary bodies is to collect mineral spectra in the laboratory and compare them with planetary data. In addition, by varying different physical parameters we can extend the existing spectral libraries such as temperature, granulometry and observation geometry on these minerals. In planetary sciences, reflectance spectroscopy in the visible and near-infrared has proven its considerable power to disclose the mineralogy of Solar System bodies (Bishop et al., 2019; Pelkey et al., 2007; Singer et al., 1979).

The reflectance spectra of minerals in the near infrared and part of mid infrared region (1 -5 µm, SWIR 1-3µm + LWIR 3-5µm) have diagnostic absorption features, due to electronic and vibration transitions, that are essential in determining surface mineralogy and consequently to understand planetary formation and evolution (Mustard and Glotch, 2019). Mineral spectral bands are closely linked to the different configurations of atoms and molecules inside the crystal structure, but they can vary in terms of positions and shapes also as a function of different environmental conditions such as temperature or pressure (e.g. (Comodi et al., 2017, 1990) which affect the structural evolutions, sometimes in anomalous way (Gatta et al., 2005). Furthermore, grain size and observation geometry strongly influence the spectral features (e.g. Beck et al., 2012; Comodi et al., 2021; De Angelis et al., 2021).

Regarding the viewing geometry, the reflectance spectra collected by spacecraft missions are generally bidirectional, that is, the incidence of the sun light has a specific angle relative to the normal direction of the surface and the reflected light has itself a proper emergence direction (Pommerol and Schmitt, 2008a). Numerous bidirectional radiative transfer models have been created that take into account the physical properties of the surface of planetary bodies, e.g., particle size and shape, roughness of the surface (Hapke, 2012, 1981); however, as surfaces are complex systems and often difficult to model, these models need to be tested with experimental data to confirm their reliability and suggest how they can be improved. For this reason, it is essential to collect laboratory Bidirectional Reflectance Distribution Function (BRDF) spectra of well-characterised samples. Furthermore, with the creation of hyperspectral cameras with increasingly high spatial resolution, the effect of surface roughness and observation geometry can be also considered.

Given the presence of surface roughness, topography and variations in morphology, the surface reflectance spectra of every Solar System bodies are affected by observation geometries, some examples include Mercury (Warell and Bergfors, 2008), Uranus' moons (Nelson et al., 1987) and asteroids (Clark et al., 2002; Magrin et al., 2012). For example on icy bodies, chaos terrain on Europa's surface, that represents resurfacing process, can be mostly identified at incidence angles > 70° (Neish et al., 2012). On Pluto's surface, the changes in viewing geometry during the New

Horizons flyby generated significant spectral changes in the N_2, CO and CH_4 absorption bands (Cruikshank et al., 2015). The dwarf planet Ceres displays a negative slope in the 0.5-2.5 µm spectral region at fresh impact craters which is related to possible changes in physical properties and composition (Stephan et al., 2017).

Up to now, several laboratory studies have analysed in detail ammonium bearing minerals using visible and near-infrared spectroscopy at various temperatures and considering different particle sizes (e.g., (Berg et al., 2016; Ciarniello et al., 2017; De Angelis et al., 2021a; Ehlmann et al., 2018; Fastelli et al., 2020; Krohn and Altaner, 1987). In all these works, the variation in viewing geometry has not been examined for the here reported samples. Exception made for the work of Ciarniello et al., 2017 that examined the BRDF effect of NH_4Cl sample. Thus, reflectance spectra of NH_4^+ minerals with different observation geometries seem to be lacking in the bibliographic record and a systematic work, dedicated to a comparative study of different effects of emergence and incidence angles on NH_4^+ features, is here proposed.

Ammonium bearing minerals have been hypothesised on the surface of primordial objects, such as comets (Poch et al., 2020), on evolved telluric planets such as Mars (Quinn et al., 2011), in some icy bodies like Ceres and Pluto (Dalle Ore et al., 2019; King et al., 1992) and asteroids, like Ryugu (Pilorget et al., 2022). The interest and identification of these minerals is linked to the possible emergence of life. Nitrogen is a key element in many biological compounds and in providing explanations for evolution and geological phenomena as they are potential environmental markers. The unambiguous detection and quantification of ammonium bearing minerals on icy bodies and small object like comets has a significant impact on the presence of either liquid salt water or phenomena such as cryovolcanism (Kargel, 1992) but also in the incorporation and evolution of nitrogen in the early Solar System (Füri and Marty, 2015). Salammoniac-NH_4Cl was identified on the surface of Ceres in relation to the absorption feature at ~2.21 µm in a bright spot area (De Sanctis et al., 2016). The genesis of this mineral is linked to the presence of either ancient brine reservoirs or brines induced by impact heating (De Sanctis et al., 2020). In fact, the formation of salammoniac is strictly related to the presence of liquid water combined with hydrothermal activity. Ammonium spectral signatures, at 1.65 and 2.2 µm, were also identified on Pluto, in a region of past extensional tectonic activity called Virgil Fossae (Cruikshank et al., 2019). These bands can be attributed to the presence of ammonium chloride salts in analogy to the one reported by Cook et al. (2018) who modelled the surface of Charon, Nyx and Hydra Pluto's satellites, observed by New Horizons, using NH_4Cl as endmembers.

Mascagnite-$(NH_4)_2SO_4$ has been suggested to be one of the rock forming minerals of the interior of Titan generated by the interactions of primordial aqueous ammonia with sulphate solutions leaking from the rocky core (Fortes et al., 2007). The Titan's internal model, from outside to inside, consists of a shell of methane clathrate, a layer of aqueous ammonium sulphates and a serpentinite core overlaid by a high pressure icy mantle (Fortes et al., 2007). Furthermore, $(NH_4)_2SO_4$ was proposed on Mars Iano Chaos area due to the presence of absorption bands at ~1.07, 1.31 and 1.57 µm consistent with its spectrum (Sefton-Nash et al., 2012). Salammoniac and mascagnite minerals are known for their low temperature phase transitions characterized by a reordering of hydrogen bonds inside the crystal structure. Salammoniac undergoes to a λ-transition defined as order-disorder type at ~242K (Levy and Peterson, 1952). After the phase transition, the mineral has a disordered CsCl-type crystal structure in which the NH_4^+ ions are distributed arbitrarily between two energy-

equivalent orientations (Wang and Wright, 1974). Mascagnite, on the other hand , undergoes a phase transition upon cooling at ~224K from a para-electric crystal structure with space group *Pnma* towards a ferro-electric crystal structure with space group $Pna2_1$ (Hasebe, 1981). In the para-electric phase, H-bonds are bifurcated and trifurcated while in the ferro-electric phase they turn in a classic, much stronger, hydrogen bond. The presence of these phase transitions may have a strong effect on the convective flow and consequently on the results of internal planetary models (Fortes and Choukroun, 2010). The two selected ammonium bearing minerals were previously characterised and tested in Fastelli et al. (2022), where the low temperature spectral behaviour was discussed. The two samples analysed in this work could represent the two most promising candidates as ammonium-bearing minerals. Also their sensitivity to solar ray alterations (Dalle Ore et al., 2019) and phase transitions should have direct consequences on the internal structure and dynamic of the bodies. If ammonium-bearing minerals are detected at the surface of icy bodies, they can play a key role as freezing compounds, depending on their abundance, that reduce the solidification temperature of water, allowing it to remain liquid in the conditions beneath the crust of frozen bodies (Neveu et al., 2017). Ammonium bearing minerals mixed with liquid H_2O can also participate in potential prebiotic reactions (e.g; Burcar et al., 2016). In addition, the spectra shown and analysed in this work will be used for future interpretation of reflectance spectra of Pluto's surface as well as on other planetary bodies such as icy satellites, asteroids, Kuiper Belt Objects (KBOs) and comets.

In this work the BRDF spectra of salammoniac and mascagnite minerals were collected with a set of three incidence angles i = 0°, 30° and 60° and nine emergence angles in the e = ±70° range, to investigate how the observation geometries influence the NH_4^+ signatures: what is the behaviour of band parameters such as their area, full width at half maximum (FWHM) and depth under varying observation geometries. The effect of geometry variation on the spectral slope was also described.

2 Materials and Methods

2.1 Ammonium bearing minerals

The two selected mascagnite-$(NH_4)_2SO_4$ and salammoniac-NH_4Cl samples were checked and characterized using X-ray powder diffraction (XRPD) technique at the Department of Physics and Geology, University of Perugia (Italy), using a Philips PW 1830 diffractometer, with a graphite monochromator, and using the CuKα radiation (λ = 1.54184 Å). Data were taken with a step scan of 0.02°/step and a step time of 20 s/step. Quantitative phase analysis were performed using the Rietveld method (Rietveld, 1969) through EXP-GUI GSAS software (Larson and Von Dreele, 1987; Toby, 2001) following the procedure described in (Guidobaldi et al., 2018). The results show that the salammoniac sample is 100 wt% pure while the mascagnite sample contains a small percentage of mohrite mineral [$(NH_4)_2Fe(SO_4)_2{\cdot}6H_2O$] about 6.4 wt% (Fastelli et al., 2022), see table 1 for details. Particle size, for the analysed samples, ranges between 32 – 80 µm. Samples were first finely ground with an agate mortar and then dry sieved.

Table 1: Compositional data, source and description for selected samples used in this study from Fastelli et al., 2022.

Mineral Name	Chemical Formula	Purity	Source
Mascagnite / Ammonium sulfate	$(NH_4)_2SO_4$	XRPD checked: small amount of mohrite 6.4 wt% [$(NH_4)_2Fe(SO_4)_2{\cdot}6H_2O$]	Pozzuoli, Italy
Salammoniac / Ammonium chloride	NH_4Cl	XRPD checked: 100 wt%	Pozzuoli, Italy

2.2 Bidirectional Reflectance Distribution Function spectra

The reflectance spectra analysed in this study were collected using the custom-made bidirectional reflectance spectro-gonio-radiometer SHINE (SpectropHotometer with variable INcidence and Emergence) (Brissaud et al., 2004) at the Cold Surface Spectroscopy facility (CSS) of the IPAG laboratory (https://cold-spectro.sshade.eu). This set up permits the collection of spectra in the visible (VIS) and near-infrared (NIR) ranges (0.35 – 4.5 µm) over a wide set of illumination (0 – 80°) and emergence angles (*e* = 0-80°). We recorded spectra over the 1 – 4.2 µm range with a spectral sampling of 10 nm up to 3.2 µm and 20 nm above with effective spectral resolution varying in 3 steps (3 gratings with fixed slit width) between 7.5 and 30 nm over the range. The illumination spot was 7.5 mm in diameter. The illumination is monochromatic and modulated (~970 Hz) with a synchronous detection so thermal emission from the sample and surrounding (not modulated) did not contribute to the reflected light (modulated) measurement (Bonnefoy 2001, Brissaud et al., 2004).

Measurements were taken in the principal plane considering a set of 3 incidence angles *i* = 0°, 30°, 60° and 9 emergence angles *e* = -70°, -60°, -40°, - 20°, 0°, 20°, 40°, 60°, 70° at room temperature. Both illumination and emergence angles are zenithal angles (measured from the normal direction to the surface) and the emergence is positive in the same quadrant as illumination in the principal plane (i.e, this corresponds to azimuth = 0° for positive emergence values, and 180° for negative

values). The phase angle g is thus simply: g = |i – e|. Furthermore, we define (*i*=0°, *e*=20°) as our reference configuration and compare the spectra measured at all other configurations with the spectrum measured at this configuration. Figure 1 presents a schematic view of the different geometrical parameters analysed.

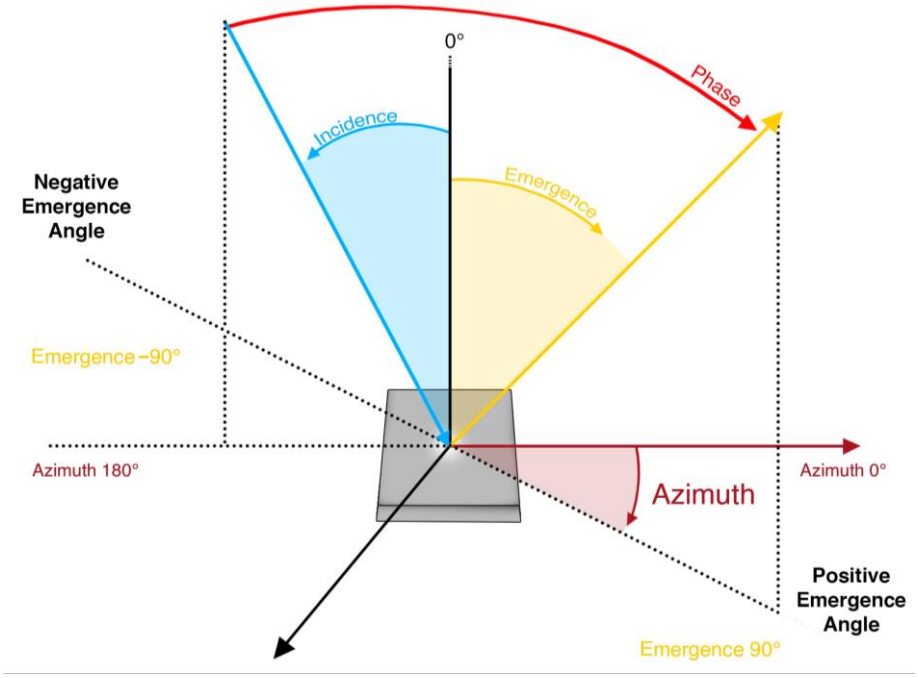

Fig. 1: Schematic representation of the different geometrical parameters analysed in this work. Pictures modified from Potin et al., 2019.

Approximately 2 g of powdered samples were put in an aluminum sample holder cup, 34 mm in diameter and 4 mm deep. The density (0.54 and 0.64 g/cm^3, respectively) and porosity (~64% for both) of the salammoniac and mascagnite samples were calculated using the measured volume and mass of the samples and the bulk density of the minerals.

The surfaces were accurately prepared, as the macroscopic structure (roughness) of the surface has a significant effect on the collected spectra and particularly on the reflectance changes between different measurement geometries (Cord et al., 2003; Pommerol and Schmitt, 2008a).

2.3 Data reduction

The recorded spectra were firstly calibrated in reflectance factor (i.e. relative to a perfectly Lambertian surface) by measuring the BRDF of a Spectralon© 99% reference target at the same set of geometries as well as an Infragold© reference target measured under the standard calibration geometry (*i*=0, *e*=30°) of the instrument (spectrally equivalent to the directional-hemispheric (i=8°) calibration provided by Labsphere). The reflectance is obtained by dividing the sample measurement by the Spectralon© measurement at the same geometry and by multiplying by the value of the spectral reflectance of Spectralon© at that geometry, from a previously calibrated absolute BRDF evaluation of the reference target (Bonnefoy, 2001). The spectral behavior of the part of the spectrum above 1.3 µm is obtained by dividing by the Infragold© measurement at the standard calibration geometry (i=0, e=30°) of the instrument and by multiplying by its spectral directional-hemispheric reflectance. The absolute reflectance of this part of the spectrum is then

obtained by adjusting (with a multiplying factor) the value of the spectrum at 1.3 µm, to that of the spectrum absolutely calibrated with Spectralon.

Regarding the study of band parameters in relation to angle variations, the procedure used to homogenize the data is detailed in the following. For each examined band, the removal of the continuum was taken equal and kept constant (same anchor point for the continuum) for all spectra. The position of the absorption bands was then measured using a second-order polynomial fit around the minimum. The depth of the band was calculated according to the following equation of: $D = (R_c - R_b)/R_c$ in which R_b is the reflectance at the centre of the band and R_c is the reflectance of the continuum at the centre of the band (Clark and Roush, 1984). The band area was determined by numerical integration over the band after continuum removal. The full width at half maximum (FWHM) was derived by cross cutting the band removed from the continuum with a horizontal line that passes through mid-depth. The band area and depth were computed for the entire band complex and not for all relative minima. More detailed information on the spectral parameter analysis procedure can be found in Comodi et al. (2021) and Fastelli et al. (2021). The spectra reduction was performed for the selected absorption bands of interest for remote sensing identification of NH_4^+- bearing minerals located at ~1.07, ~1.3, ~1.58, ~2.07, ~2.17 and ~3.03 µm

3 Results

Figures 2 and 3 report the bi-directional reflectance spectra of the two selected ammonium bearing minerals mascagnite and salammoniac, respectively, collected at different illumination-emergence geometries. Table 2 provides the absorption bands positions at reference geometry for this work (*i*=0°., *e*=20°.) analysed in this work and their assignment.

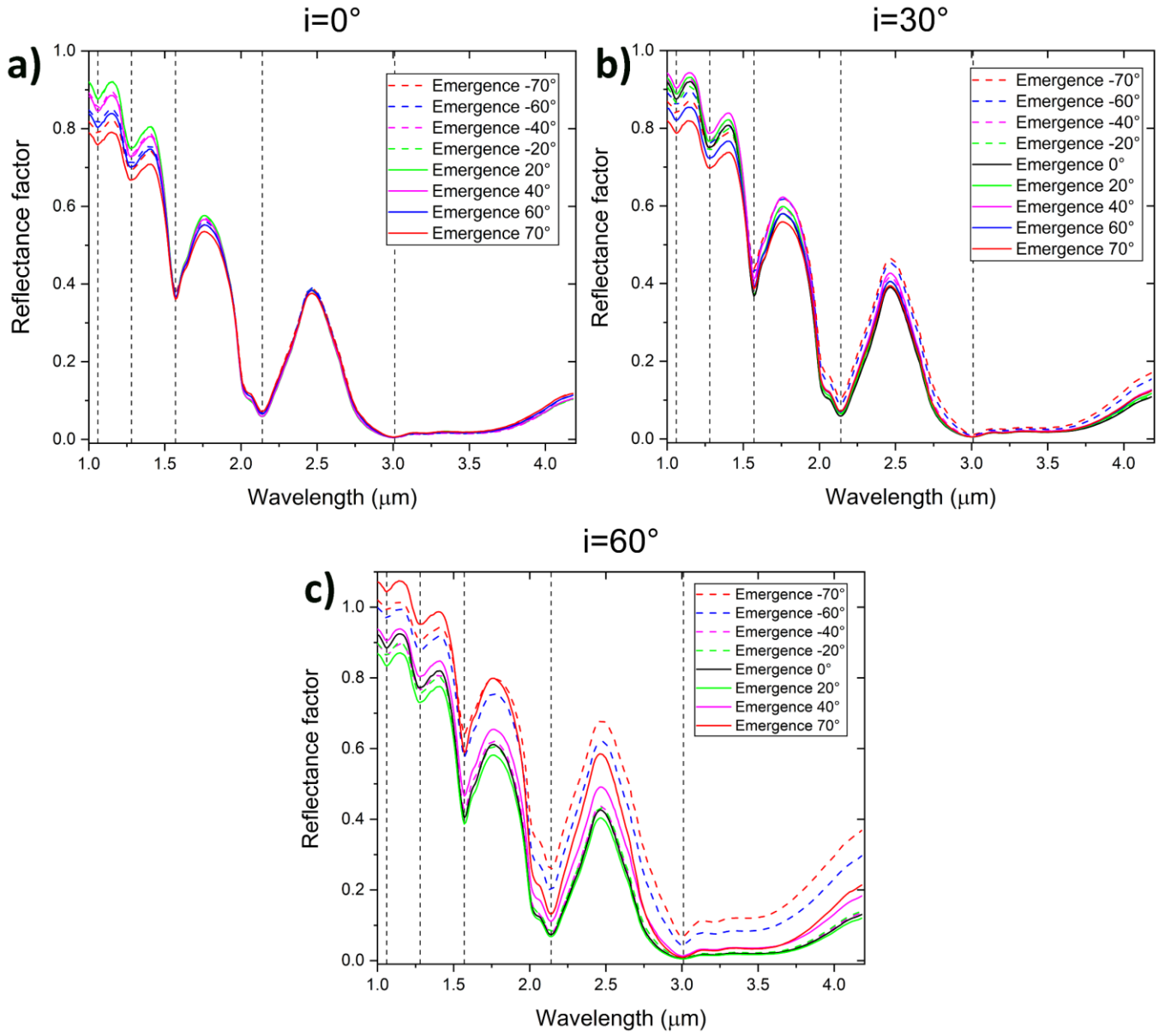

Fig. 2: *BRDF spectra of the Mascagnite-$(NH_4)_2SO_4$ sample. Each of the three plots presents spectra measured at zenithal incidence angle 0° (a), 30° (b) and 60° (c) and different emergence angles in the ± 70° range. Spectra with negative emergence "e" angle (i.e. azimuth = 180°) are reported with dashed lines retaining the same colour for same absolute value of the positive emergence (i.e. azimuth = 0°). BRDF data at 1.06, 1.28, 1.57, 2.14 and 3.01 μm wavelengths are analysed (marked by vertical dash lines).*

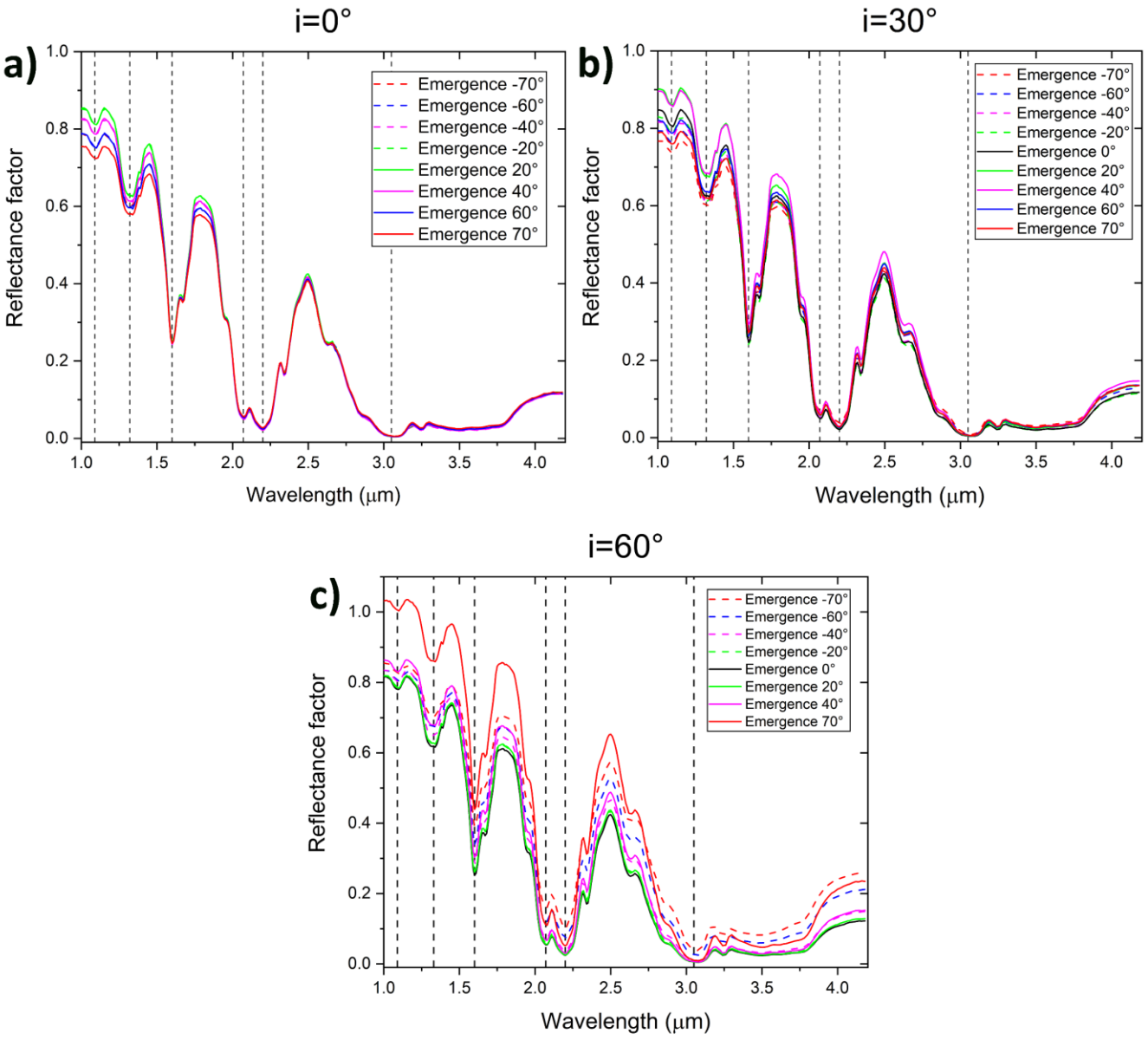

Fig. 3: *BRDF spectra of the Salammoniac-NH_4Cl sample. Each of the three plots presents spectra measured at zenithal incidence angle 0° (a), 30° (b) and 60° (c) and different emergence angles in the ± 70° range. Spectra with negative emergence "e" angle (i.e. azimuth = 180°) are reported with dashed lines retaining the same colour for same absolute value of the positive emergence (i.e. azimuth = 0°). BRDF data at 1.09, 1.33, 1.62, 2.06, 2.2 and 3.05 μm wavelengths are analysed (marked by vertical dash lines).*

Table 2: Positions and vibration mode assignments of the reflectance spectra collected with reference geometry (i=0°; e=20°) for the selected bands analysed in this work. Intensity labels are: *w* = weak, *m-s* = moderately-strong, *m*=medium and *s*=strong. Band assignments were made following (Berg et al., 2016; Fastelli et al., 2022; Krohn and Altaner, 1987).

Mineral	Band position (µm)	Vibrational modes	Intensity
Mascagnite $(NH_4)_2SO_4$	1.06	$NH_4^+ 3\nu_3$	*w*
	1.28	$NH_4^+ 2\nu_3 + \nu_4$	*w*
	1.57	$NH_4^+ 2\nu_3$	*m-s*
	2.18	$NH_4^+ \nu_3 + \nu_4$	*s*
	3.01	$NH_4^+ \nu_3$	*s*
Salammoniac NH_4Cl	1.09	$NH_4^+ 3\nu_3$	*w*
	1.32	$NH_4^+ 2\nu_3 + \nu_4$	*w*
	1.62	$NH_4^+ 2\nu_3$	*m-s*
	2.06	$NH_4^+ \nu_2 + \nu_3$	*s*
	2.2	$NH_4^+ \nu_1 + \nu_4$ and/or $NH_4^+ \nu_3 + \nu_4$	*s*
	3.05	$NH_4^+ \nu_3$	*s*

The absorption bands identified in the spectra of both samples in the 1-2.5 µm range are mainly due to overtones and combinations of the fundamental internal vibrations of the NH_4^+ group. These features are located at ~1.07, ~1.3, ~1.58, ~2.07, ~2.17 µm. On the right side of the spectra, between 2.8 and 3.8 µm, we notice several saturated and overlapping NH_4^+ bands except for the salammoniac sample which shows two clear features at 3.05 and 3.25 µm. Due to the high hygroscopicity of these minerals, although they were kept inside a desiccator before measurement, some spectral features of adsorbed H_2O are present at ~1.47, ~1.94, ~2.62, ~2.83 and ~3.0 µm that, in some cases, overlap with the NH_4^+ bands. In addition, the water molecules absorb in wide wavelength ranges around each of the central wavelengths listed above. These positions refer to spectra collected with the reference configuration geometry (*i*=0°, *e*=20°).

Ammonium sulphates NH_4^+ absorption features are located near 1 µm, at ~1.56 µm, and ~2.2 µm. Over 3 µm, bands are broad and saturated at reference configuration geometry. Ammonium chloride (NH_4Cl) presents clear absorption features in the 1.0 – 2.12 µm range with distinct absorption feature at 1.09, 1.33, 1.38 1.62 and 1.67 µm and three bands in the 2- 2.4 µm range attributed to NH_4^+ groups.

The selected absorption bands can be ascribed to the following detailed vibrational modes of NH_4^+ group: ~ 1.09 µm ($NH_4^+ 3\nu_3$); ~1.3 µm ($NH_4^+ 2\nu_3 + \nu_4$); ~ 1.6 µm ($NH_4^+ 2\nu_3$); ~2.02 µm ($NH_4^+ \nu_2 + \nu_3$); ~2.2 µm ($NH_4^+ \nu_3 + \nu_4$); ~ 3 µm ($NH_4^+ \nu_3$) (Berg et al., 2016; Fastelli et al., 2021; Krohn and Altaner, 1987).

The effect of increase in reflectivity towards high incidence and emergence angles due to 'forward scattering' is evident from the plots shown in Figures 2 and 3 for both samples. In fact, the highest reflectance values are found at the highest incidence and negative emergence angles (high phase angles). A second clear effect is the reduction of the negative slope with respect to wavelength in the continuum of salammoniac and mascagnite samples at high emergence and incidence angles. Spectra acquired at an incident angle of 0° are characterised by a lower variability of this parameter relative to emergence angles. On the contrary, spectra collected at an incident angle of 60° show

significant variations depending on the angle of emergence, in particular at both low (g ≤ 20°, i.e., e = 40 - 70°) and high phase angles (g > 100°, i.e., e < -40°).

Another interesting behaviour is shown by the NH_4^+ absorption feature in mascagnite sample located at ~3.0 µm. In particular, as the incident and emergence angles increase, these features become less saturated and better defined (Figure 2). In order to clarify the behaviour of the selected bands, for both samples, figures 4 and 5 show the variation in reflectance factor in relation to phase angles (g).

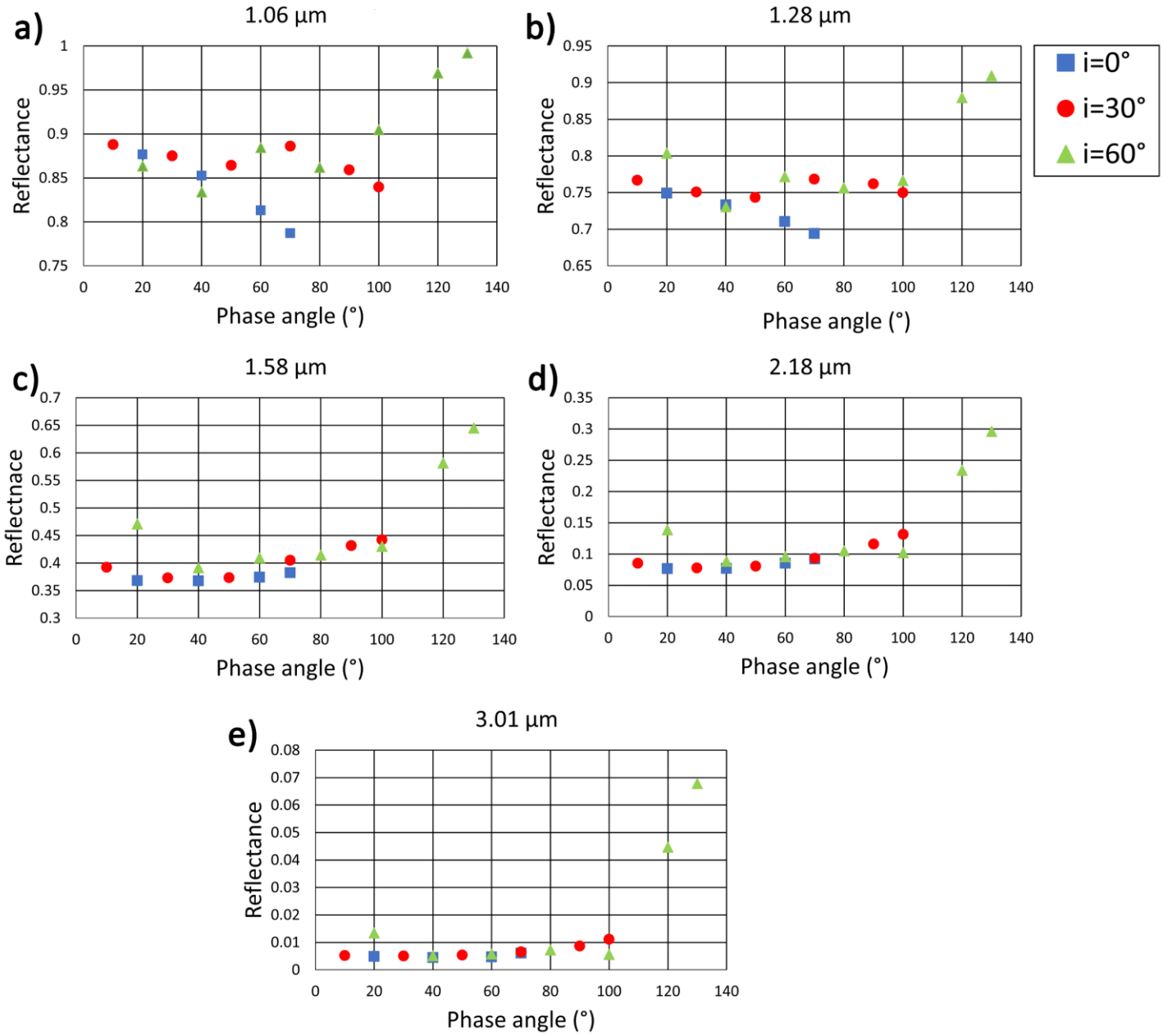

Figure 4: Reflectance factor as a function of the phase angle g for mascagnite-$(NH_4)_2SO_4$ sample. Colored symbols refer to each incidence angle: blue squares (i = 0°), red circles (i = 30°) and green triangles (i = 60°). Panels a, b, c, d and e correspond to 1.06, 1.28, 1.58, 2.18 and 3.01 µm wavelengths, respectively. Note the different scale of the y axis.

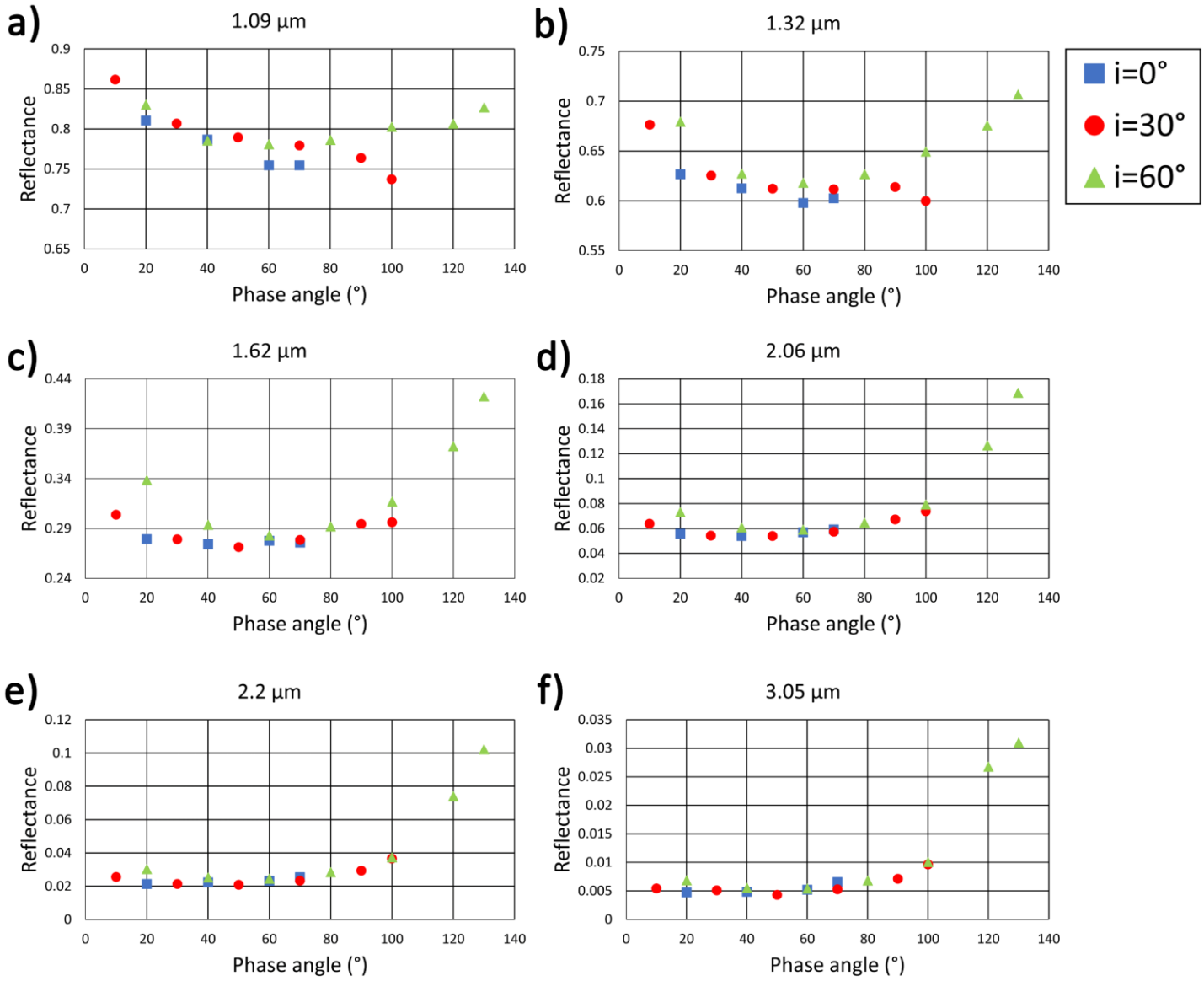

Figure 5*: Reflectance factor as a function of the phase angle g for salammoniac-NH_4Cl sample. Colored symbols refer to each incidence angle: blue squares (i = 0°), red circles (i = 30°) and green triangles (i = 60°). Panels a, b, c, d, e and f correspond to 1.09, 1.32, 1.62, 2.06, 2.2 and 3.05 µm wavelengths, respectively. Note the different scale of the y axis.*

3.1 BRDF spectra and geometry

The measured reflectance factors at different incident zenithal angles are shown in polar plots in Figures 6 and 7 for mascagnite and salammoniac, respectively, where the BRDF appears as a half of a circle (with value of 1 for a perfectly Lambertian surface) and gives a simple overview of the different viewing geometry effect. BRDF is plotted in polar coordinates at 1.06, 1.28, 1.57, 2.18 and 3.01 µm for mascagnite (Figure 6) and at 1.09, 1.32, 1.60, 2.06, 2.2 and 3.05 µm for salammoniac (Figure 7). These wavelengths correspond to the minima positions of NH_4^+ absorption bands. The reported BRDF polar plots show a backscattering effect around the incidence quadrant (small phase angles) and forward scattering at high phase angles. The increase of reflectance values as phase angle decreases is due to the shadows hiding opposition effect (SHOE), *i.e.*, at angles close to 0° the effect of shadows between particles is almost negligible and the reflectance in the direction of incidence increases (Hapke, 1986). The samples analysed were manually powdered and sieved,

reducing the distribution of grain sizes. Thanks to the accurate sample preparation the roughness is at the level of a few grain sizes. However, the SHOE effect is affected by the intrinsic roughness of powder that creates shadowing of one particle over another (Pommerol and Schmitt, 2008a; Potin et al., 2019). Mascagnite and salammoniac present relatively similar behaviours of the BRDF and show an increase in reflectivity towards high phase angles (for $i \geq 30°$ and $e \geq 60°$) especially for absorption bands over 2 µm. In fact, smaller particles compared to those with larger dimensions, producing a larger number of reflections at their interface, have more pronounced forward scattering than larger particles, except when very small particles form fluffy aggregates, which is not the case of our samples which are slightly packed to get a flat surface. Due to these phenomena, the two samples studied show a non-Lambertian behaviour.

The reflectance values variations for the analysed bands are reported in table 3 and 4 for mascagnite and salammoniac, respectively. For the mascagnite sample, the weak bands located at 1.06 and 1.28 µm have slightly decreased reflectance values, for $i = 0°$ and 30° and large emergence angles, $e \geq \pm 40°$, from 0.87 ($i = 0°$; $e = 20°$) to 0.75 ($i = 0°$; $e = -70°$) (Figures 6 a-b); The moderately strong spectral feature at 1.58 µm, shows almost no change in reflectance with emergence angle for nadir illumination (i = 0°), but at i = 30° the reflectance starts to increase at high phase angle (> 70°, i.e., e < -40°, Figure 6 c). This trend is growing with the strong band at 2.18 µm and the very strong one at 3.01 µm which show an increase in the reflectance values for increasing phase angles at both i = 0° and 30°, a behaviour opposite to that of the 1.06 and 1.28 µm features. Furthermore, at high incidence angle (i = 60°) all bands display a clear reflectance increase at both low ($g \leq 20°$, i.e., e = 40 - 70°) and high phase angles (g > 100°, i.e., e < -40°).

At low and high phase angles the relative magnitude of the increase in reflectance (relative to values at medium phase angle) rapidly grows with the absolute band strength. For the strongest band around 3 µm we can observe the highest increase of the reflectance values, by a factor more than 3 at low phase angle, and by more than an order of magnitude at high phase angles. On the other hand the weakest 1.06 and 1.28 µm features display only moderate increase in band center reflectance values, by factors of less than 1.3.

The BRDF spectra of salammoniac sample exhibit similar behaviour to mascagnite. The spectral features at 1.09, 1.58 and 1.62 µm are those characterized by less variability, in terms of reflectance reduction, with the phase angle variation (Figures 7 a-b-c). These spectral features show the maximum reflectance value for $i = 60°$ and $e = 70°$. The bands located at 2.06, 2.2 and 3.05 µm have increased reflectance values starting from $i = 30°$ and $e \geq 40°$ (Figures 7 d-e-f). Maximum reflectance values are obtained for observation geometry configurations corresponding to $i = 30°$ and $e = 70°$.

Table 3: Reflectance behaviour of the analysed bands as a function of incidence (*i*) and emergence (*e*) angles for the mascagnite sample. The arrows indicate the increase (↑) or decrease (↓) variations with respect to the *e* = 0° angle. The symbol (-) indicates no variations.

Bands position (µm)	**i = 0°**								
	-70°	**-60°**	**-40°**	**-20°**	**0°**	**20°**	**40°**	**60°**	**70°**
1.06	↓	↓	↓	-		-	↓	↓	↓
1.28	↓	↓	↓	-		-	↓	↓	↓
1.57	↑	↑	↓	-		-	↓	↓	↓
2.18	↑	↑	↑	-		-	↑	↑	↑
3.01	↑	↑	↓	-		-	↓	↑	↑
	i = 30°								
1.06	↓	↓	↑	↑		↑	↑	↓	↓
1.28	↓	↓	↑	-		↑	↑	↓	↓
1.57	↑	↑	↑	-		↑	↑	↓	↓
2.18	↑	↑	↑	-		↑	↑	↑	↑
3.01	↑	↑	↑	↑		↑	↑	-	↑
	i = 60°								
1.06	↑	↑	↑	↓		↓	↑		↑
1.28	↑	↑	↑	↓		↓	↑		↑
1.57	↑	↑	↑	↑		↓	↑		↑
2.18	↑	↑	↑	↑		↑	↑		↑
3.01	↑	↑	↓	↑		↓	↑		↑

Table 4: Reflectance behaviour of the analysed bands as a function of incidence (i) and emergence (e) angles for the salammoniac sample. The arrows indicate the increase (↑) or decrease (↓) variations with respect to the *e* = 0° angle. The symbol (-) indicates no variations.

Bands position (µm)	**i = 0°**								
	-70°	**-60°**	**-40°**	**-20°**	**0°**	**20°**	**40°**	**60°**	**70°**
1.09	↓	↓	↓	-		-	↓	↓	↓
1.32	↓	↓	-	-		-	↓	↓	↓
1.62	↑	↑	↓	-		-	↓	↑	-
2.06	↑	↑	↓	-		-	↓	↑	↑
2.2	↑	↑	↑	-		-	↑	↑	↑
3.05	↑	↑	↑	-		-	↑	↑	↑

	i = 30°								
1.09	↓	↓	↓	-		↑	↑	-	↓
1.32	↓	↓	-	-		↑	↑	↓	↓
1.62	↑	↑	-	↓		↑	↑	↑	↑
2.06	↑	↑	↑	-		↑	↑	↑	↑
2.2	↑	↑	↑	-		↑	↑	↓	-
3.05	↑	↑	↑	↑		↑	↑	↑	↑
	i = 60°								
1.09	↓	↑	↑	↑		↑	↑		↑
1.32	↓	↑	↑	↑		↑	↑		↑
1.62	↑	↑	↑	↑		↑	↑		↑
2.06	↑	↑	↑	↑		↑	↑		↑
2.2	↑	↑	↑	↑		↑	↑		↑
3.05	↑	↑	↑	↑		↑	↑		↑

342

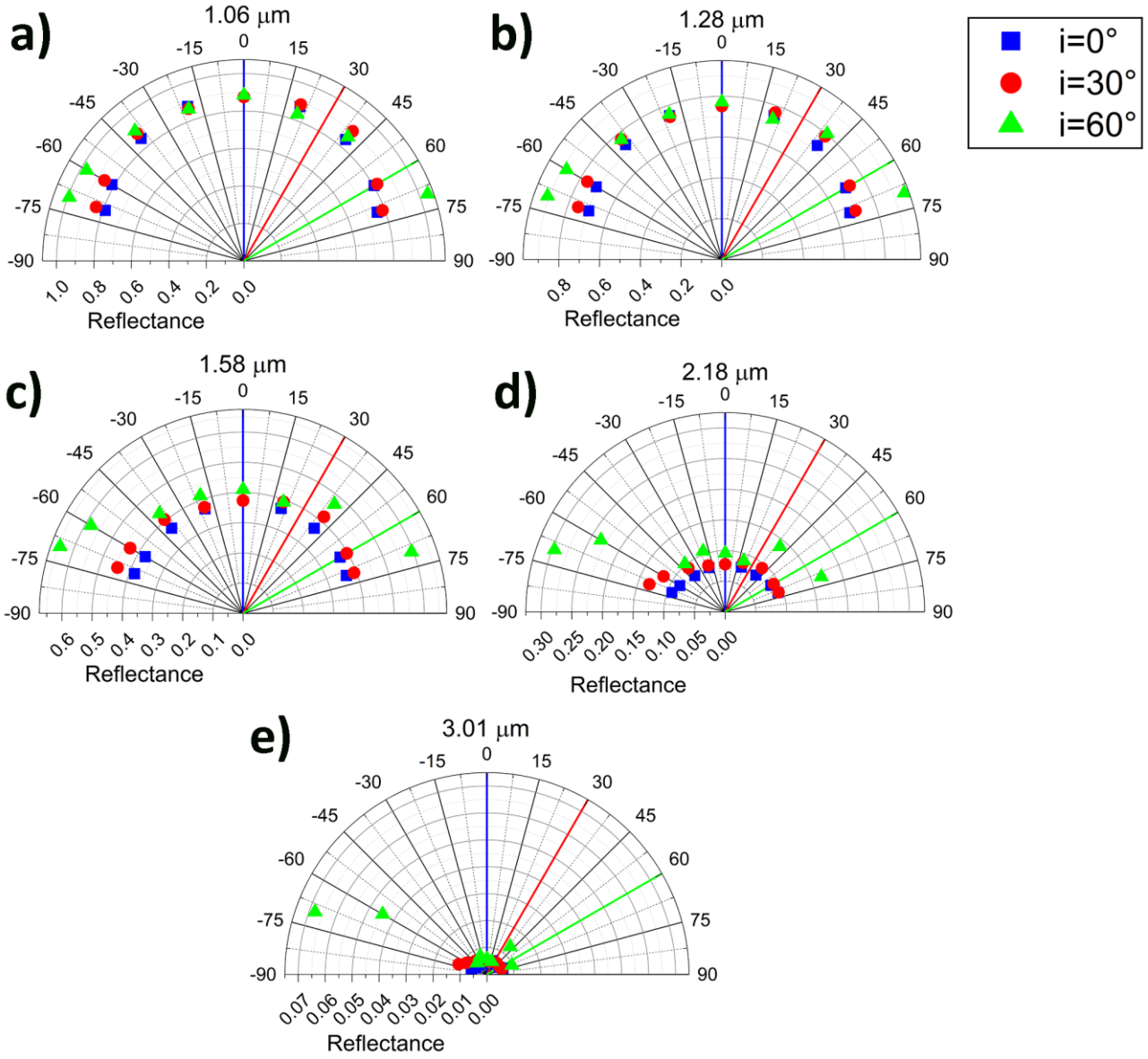

Fig.6. Polar plots in the principal plane of bidirectional reflectance distribution function for mascagnite-$(NH_4)_2SO_4$ sample. Colored symbols and lines refer to each incidence angle: blue squares (i = 0°), red circles (i = 30°) and green triangles (i = 60°). Positive emergence angles correspond to azimuth = 0° (back-scattering quadrant) and negative values to azimuth = 180° (forward-scattering quadrant). Angles are given in degrees. Note the different scales of the axis. Panels a, b, c, d and e correspond to 1.06, 1.28, 1.58, 2.18 and 3.01 μm wavelengths, respectively.

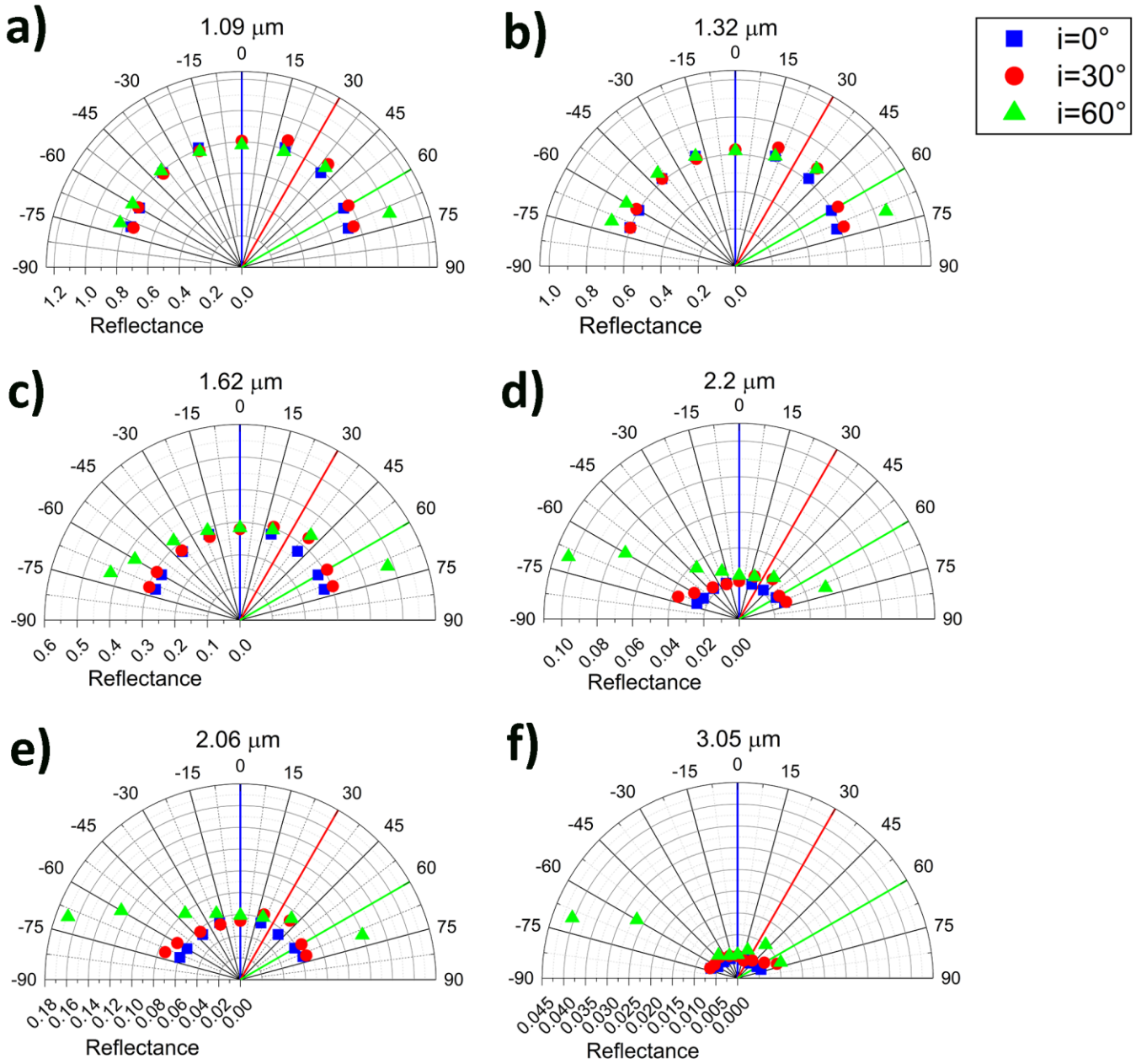

Fig. 7: *Polar plots in the principal plane of bidirectional reflectance distribution function for mascagnite-$(NH_4)_2SO_4$ sample. Colored symbols and lines refer to each incidence angle: blue squares (i = 0°), red circles (i = 30°) and green triangles (i = 60°). Positive emergence angles correspond to azimuth = 0° (back-scattering quadrant) and negative values to azimuth = 180° (forward-scattering quadrant). Angles are given in degrees. Note the different scales of the axis. Panels a, b, c, d, e and f correspond to 1.09, 1.32, 1.62, 2.06, 2.2 and 3.05 μm wavelengths, respectively.*

3.2 Effect of observation geometry on bands parameters

For the two analysed samples, the bands depth, area and FWHM were analysed following Comodi et al. (2021) as reported in the methods section (section 2). The bands area, depth and FWHM of mascagnite sample are reported in Figures 8, 9, and 10, respectively, whereas the bands area, depth and FWHM of salammoniac sample are given in Figures 11, 12 and 13, respectively. The absorption

features detected for the mascagnite and salammoniac samples are consistent with previous published spectra (e.g., Berg et al., 2016).

The collected data show that the band depth and area are strongly influenced by the viewing angle (Figures 8, 9 and 11, 12). On the contrary, the position of the bands remains unchanged. Similar works (e.g.; Beck et al., 2012; Pommerol and Schmitt, 2008b; Potin et al., 2019) report that variation in the observation geometry corresponds to a decrease in band depth at higher phase angles due to the increase in photons scattered out of the sample before penetrating a few grains deep below the surface. Our measurements show a decrease in depth values with increasing incidence and emergence angles as reported in literature for $e \geq 40°$. However, an opposite trend can be observed for the absorption bands located over 2 µm. For both mascagnite (Figures 8 and 9) and salammoniac samples (Figures 11 and 12), for $i = 60°$ and *(i)* and *(e)* angles greater than 40°, the band depth and consequently the area tend to increase their values. This is particularly marked on the ~2.2 ($\nu_3 + \nu_4$) and ~3.0 (ν_3) µm features in both minerals.

Regarding the 3 µm band, it exhibits a broad and shallow shape for variable emergence angles collected with i=0°. This spectral feature reveals a fine structure with increasing incidence and emergence angles. For incidence angle equal to 60° and emergence angles ≥ 60°, the 3 µm feature is well defined and clearly detectable (Figures 6e and 7f).

Finally, the FWHM parameter shows no clear trend with the change in observation geometry (Figures 10 and 13). The absence of a possible trend for this band parameter was also found when varying other physical parameters such as temperature and particle size (e.g.; De Angelis et al., 2021, 2019). However, our data for the 2.18 µm bands of mascagnite sample (Fig. 7d) and the 1.62 µm bands of salammoniac (Fig. 10c) display clear trends with changing viewing geometry.

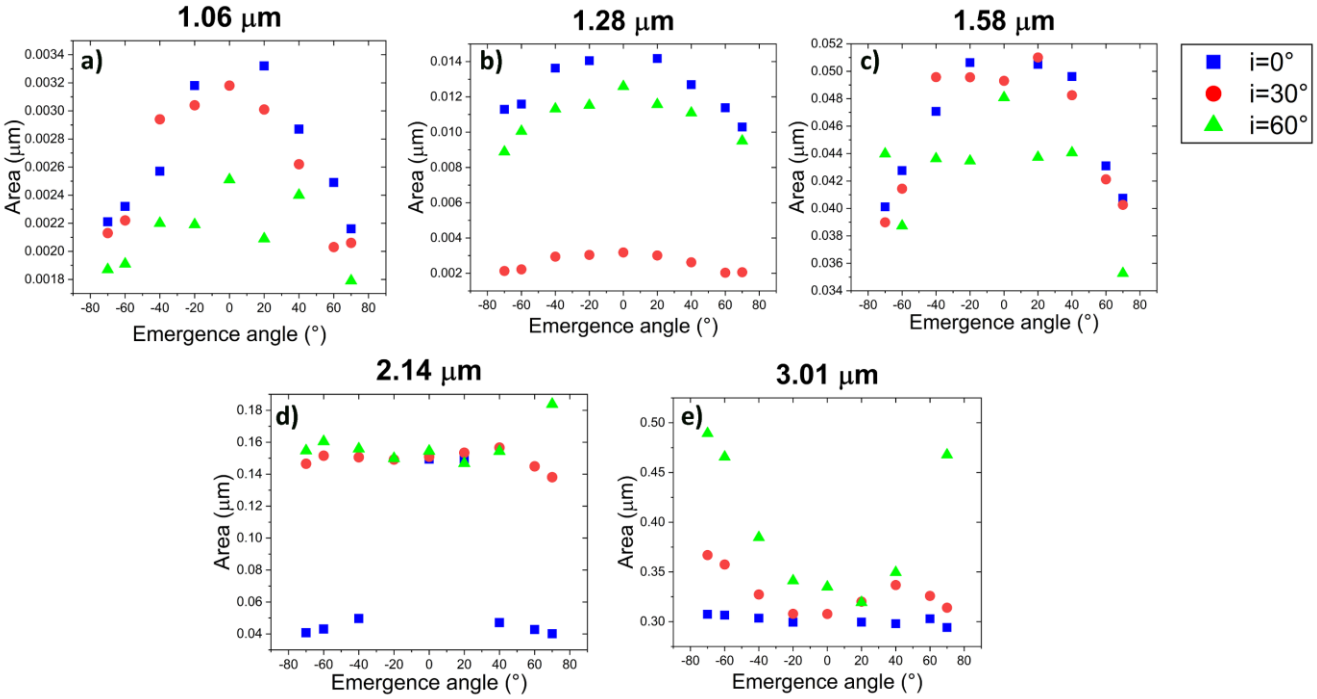

Fig. 8: Band area of the 1.06 (a), 1.28 (b), 1.58 (c), 2.18 (d) and 3.01 (e) µm absorption features of mascagnite sample for different incident and emergence angles. Note the different scales of the y axis.

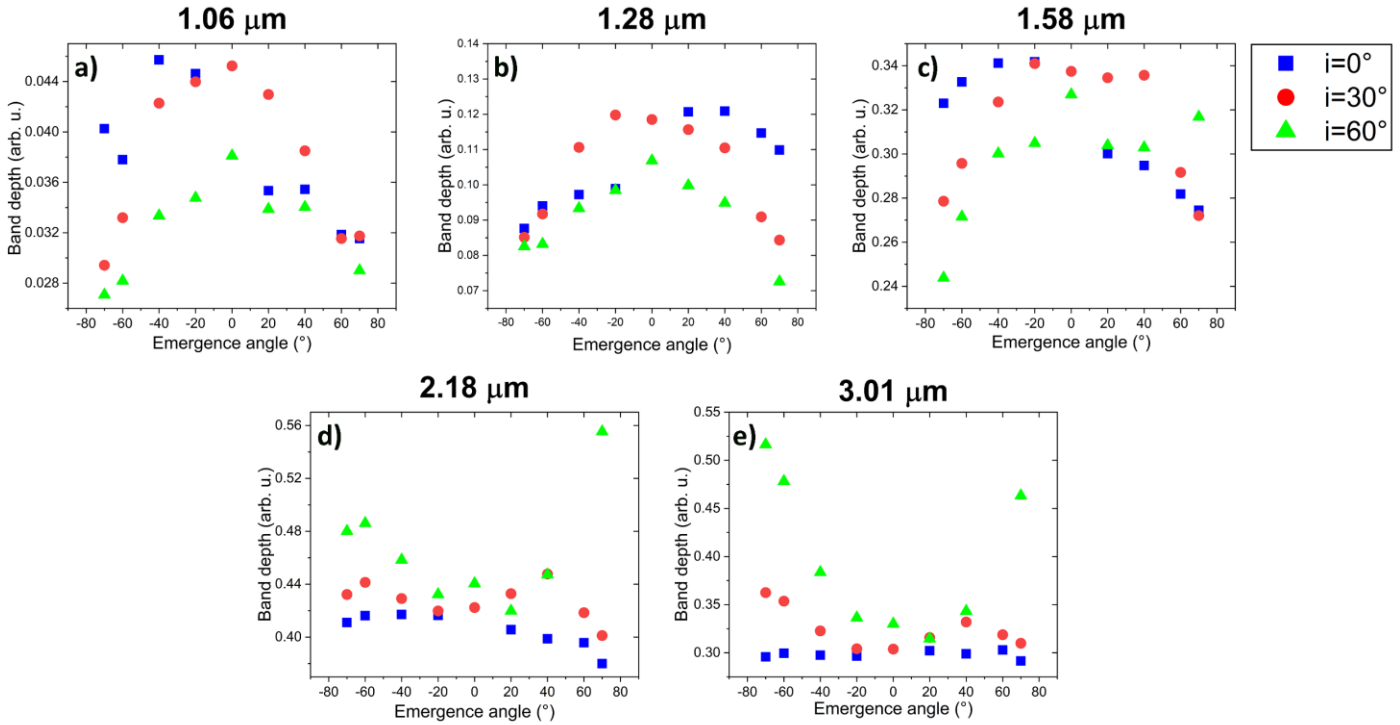

Fig. 9: Band depth of the 1.06 (a), 1.28 (b), 1.58 (c), 2.18 (d) and 3.01 (e) µm absorption features of mascagnite sample for different incident and emergence angles. Note the different scales of the y axis.

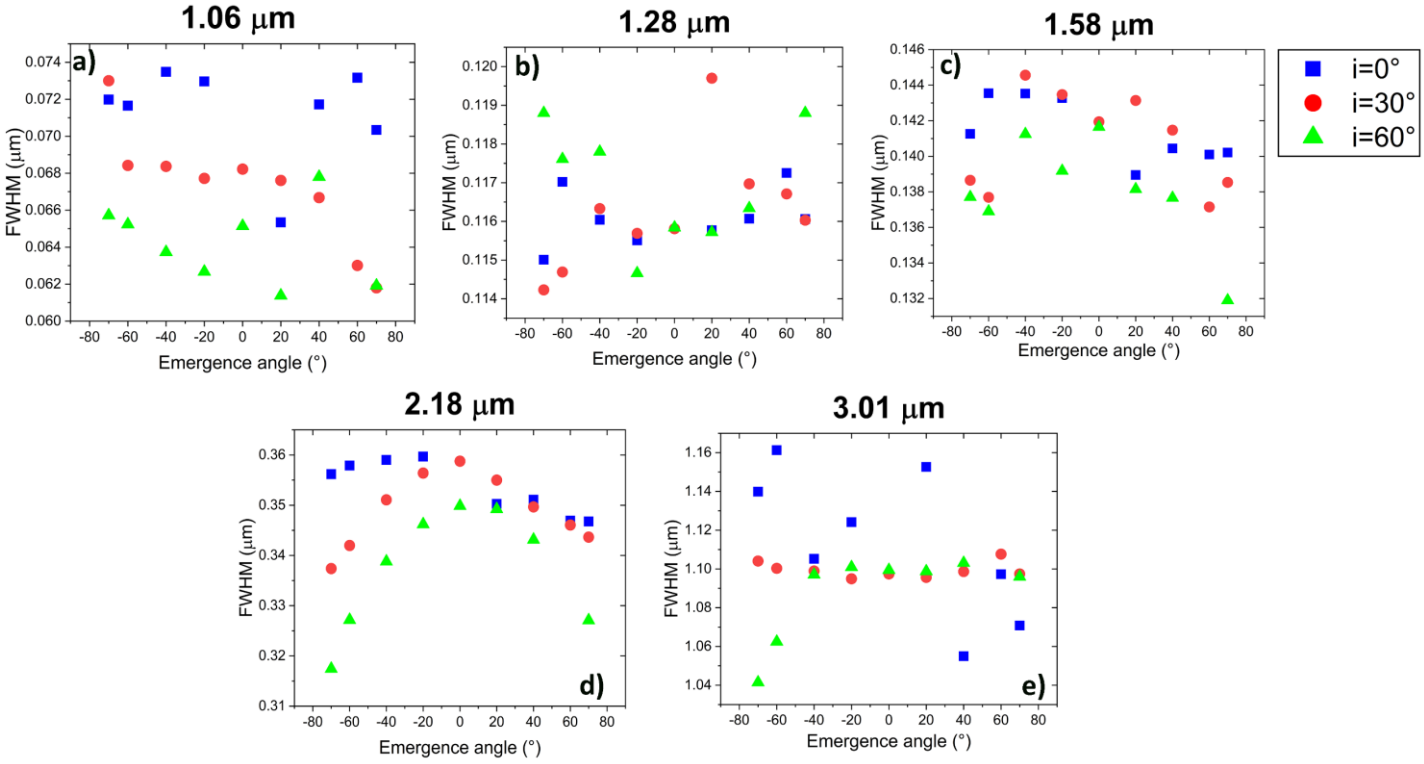

Fig.10: Band FWHM of the 1.06 (a), 1.28 (b), 1.58 (c), 2.18 (d) and 3.01 (e) µm absorption features of mascagnite sample for different incident and emergence angles. Note the different scales of the y axis.

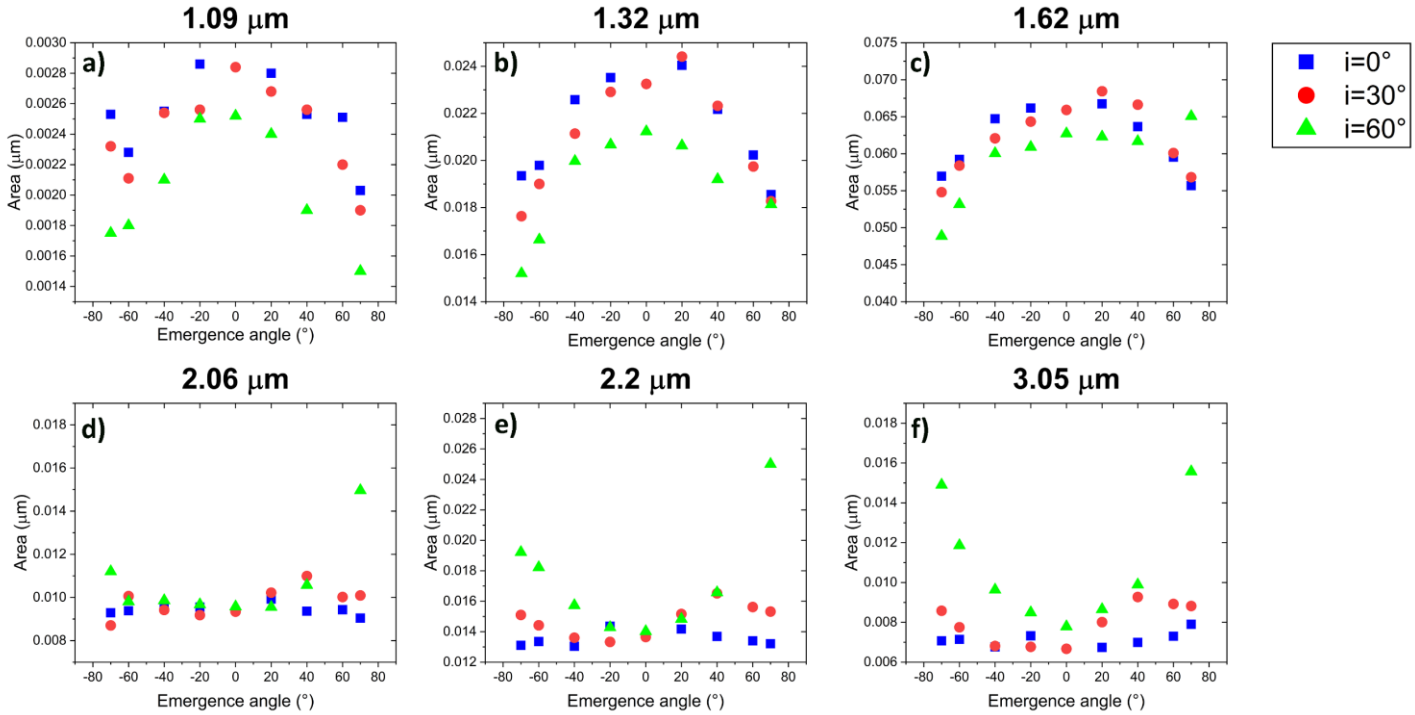

Fig.11: Band area of the 1.09 (a), 1.32 (b), 1.62 (c), 2.06 (d), 2.2 (e) and 3.05 (f) μm absorption features of salammoniac sample for different incident and emergence angles. Note the different scales of the y axis.

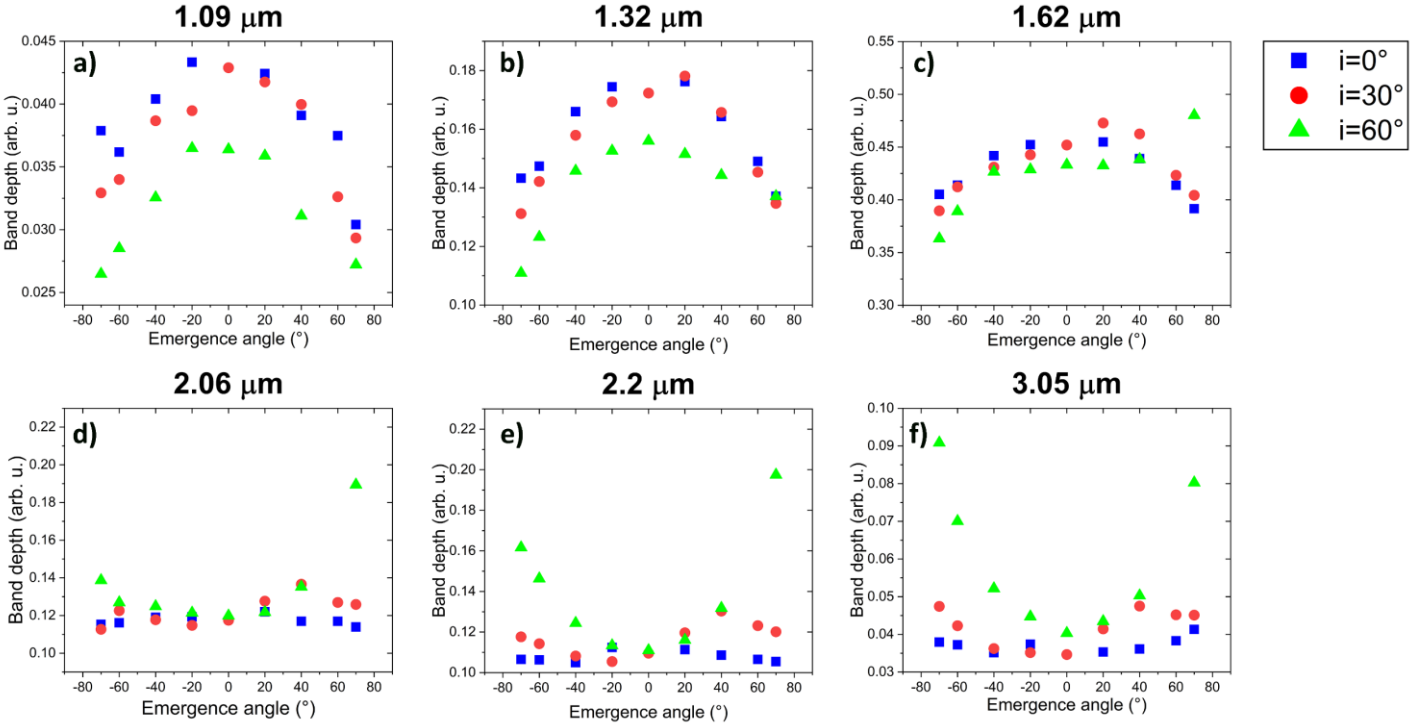

Fig. 12: Band depth of the 1.09 (a), 1.32 (b), 1.62 (c), 2.06 (d), 2.2 (e) and 3.05 (f) μm absorption features of salammoniac sample for different incident and emergence angles geometry. Note the different scale of the y axis.

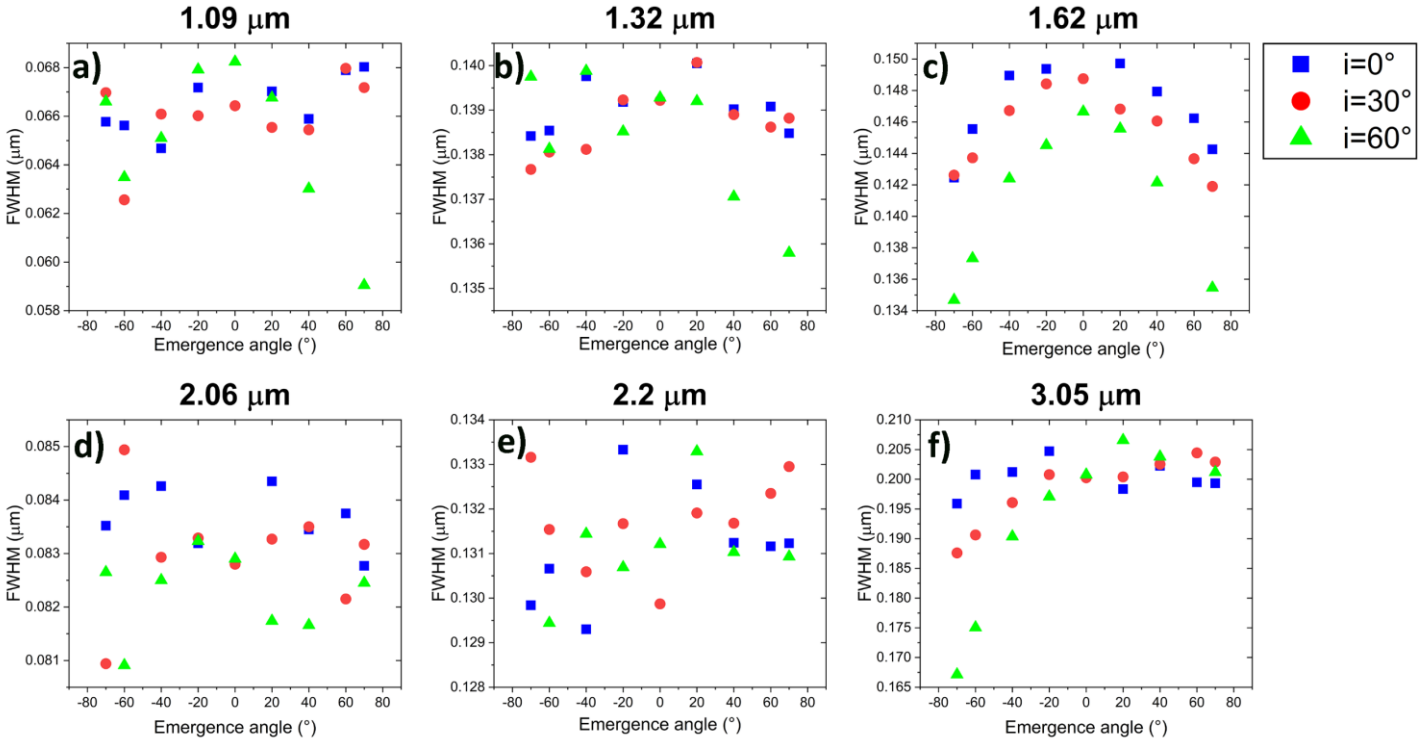

406

407 *Fig.13: Band FWHM of the 1.09 (a), 1.32 (b), 1.62 (c), 2.06 (d), 2.2 (e) and 3.05 (f) μm absorption*
408 *features of salammoniac sample for different incident and emergence angles. Note the different*
409 *scales of the y axis.*

3.3 Spectral slope vs geometry

For the quantitative determination of the slope parameter, the methodology reported in Fornasier et al. (2015) was followed. The spectral slope can be computed as the ratio of two reflectance values given at two different wavelengths (Schröder et al., 2014). For each collected spectrum, three slopes were determined, taking into account the reflectance values located at 1.15 - 1.4 μm, 1.4 – 1.76 μm and 1.76 – 2.46 μm; these three regions were chosen as no absorption feature occurs within them. The value of the normalized spectral slope is calculated as the ratio between the reflectance values at 1.4 μm (*1*) and at 1.15 μm (*2*) here reported as an example. The same operation was made for the other two slopes:

$$norm.\,slope\ (\%\ \mu m^{-1}) = 2 * \frac{(R1-R2)}{[(R1+R2)*(\lambda 1-\lambda 2)]}$$

where R and λ indicate the values of reflectance and wavelength (μm), respectively.

The variation of the spectral slope and the emergence angles is reported in Figure 14 for both salammoniac and mascagnite. The reflectance spectra of salammoniac (Figure 14a) have a similar negative slope (blueing) to those of mascagnite (Figure 14b). At low emergence angle, mascagnite spectra have slope value of -0.53 %μm^{-1}, whereas salammoniac displays slope value of -0.77 %μm^{-1}. At incidence (i = 0) and emerges (e = ±70°) angles, the slope of mascagnite sample reaches the mean value of -0.30 %μm^{-1} compared to -0.45 %μm^{-1} for the salammoniac spectra. Generally, the blueing effect is linear with increasing angles of incidence and emergence. The spectral slope is strongly affected by the surface particle density and texture (Binzel et al., 2015) as well as by the different grain size distribution and chemical composition (De Angelis et al., 2014; Pisello et al., 2022a, 2022b). Regarding the variation of the slope with different grain sizes, we expect a change from positive (red) to negative (blue) values as the grain size increases.

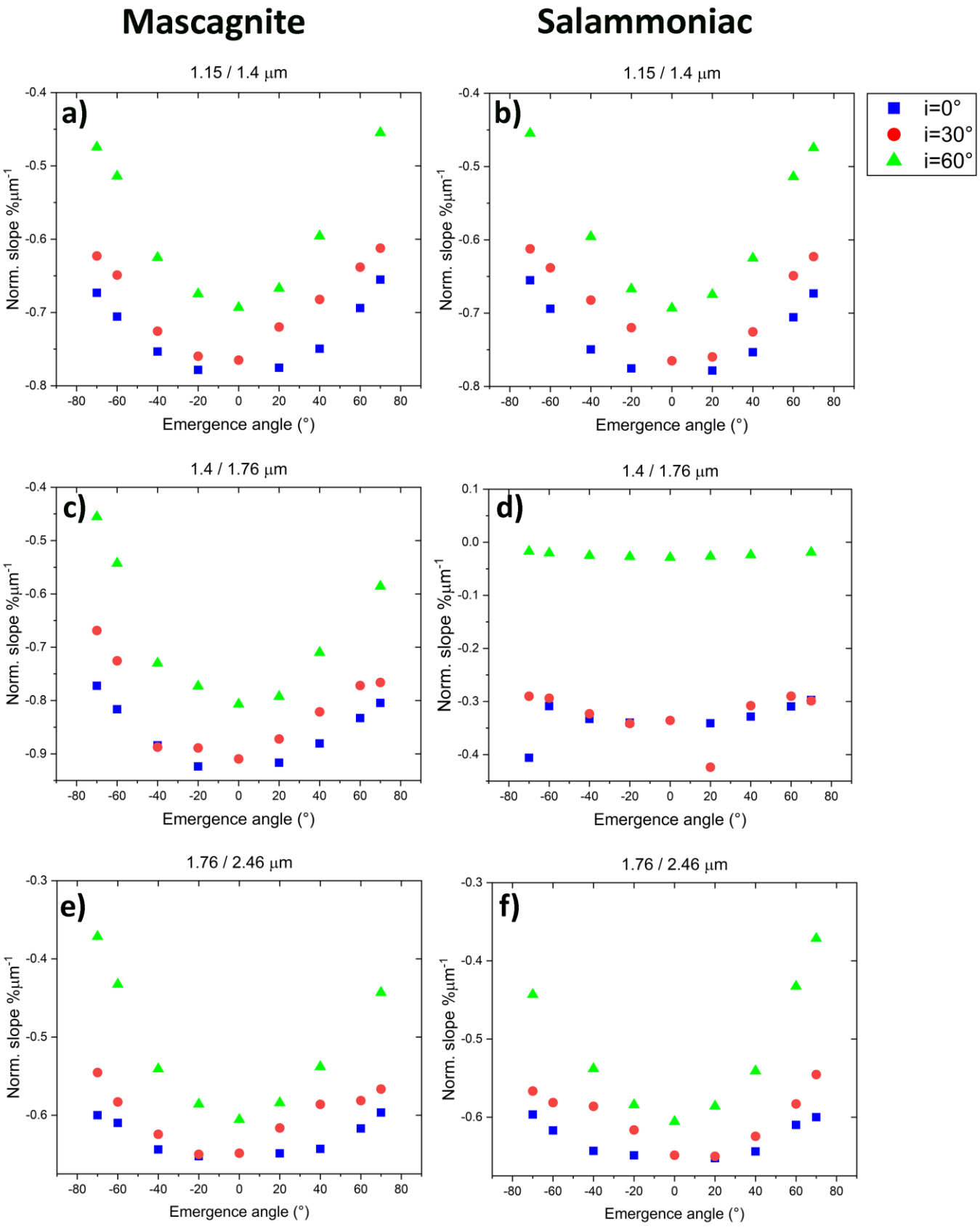

Fig.14: *Effect of the geometry variation on the spectral slope of the reflectance spectra of mascagnite (left column a-c-e) and salammoniac samples (right column b-d-f).*

4. Discussions

4.1 Quantification of viewing geometry variations

To numerically quantify the effect of the emergence angle variations on the measured reflectance spectra, we calculated the difference between reflectance with e = 20° with respect to the other values of e. For the selected bands analysed in the previous sections, the absolute value of (R_e – $R_{e=20}$) was divided by $R_{e=20}$ to express the ratio of deviation with respect to the reference geometry observation *(i=0° and e=20°)*. Each deviation value for mascagnite e salammoniac samples is plotted in Figures 15 and 16, respectively, for i= 0°; 30°; 60°.

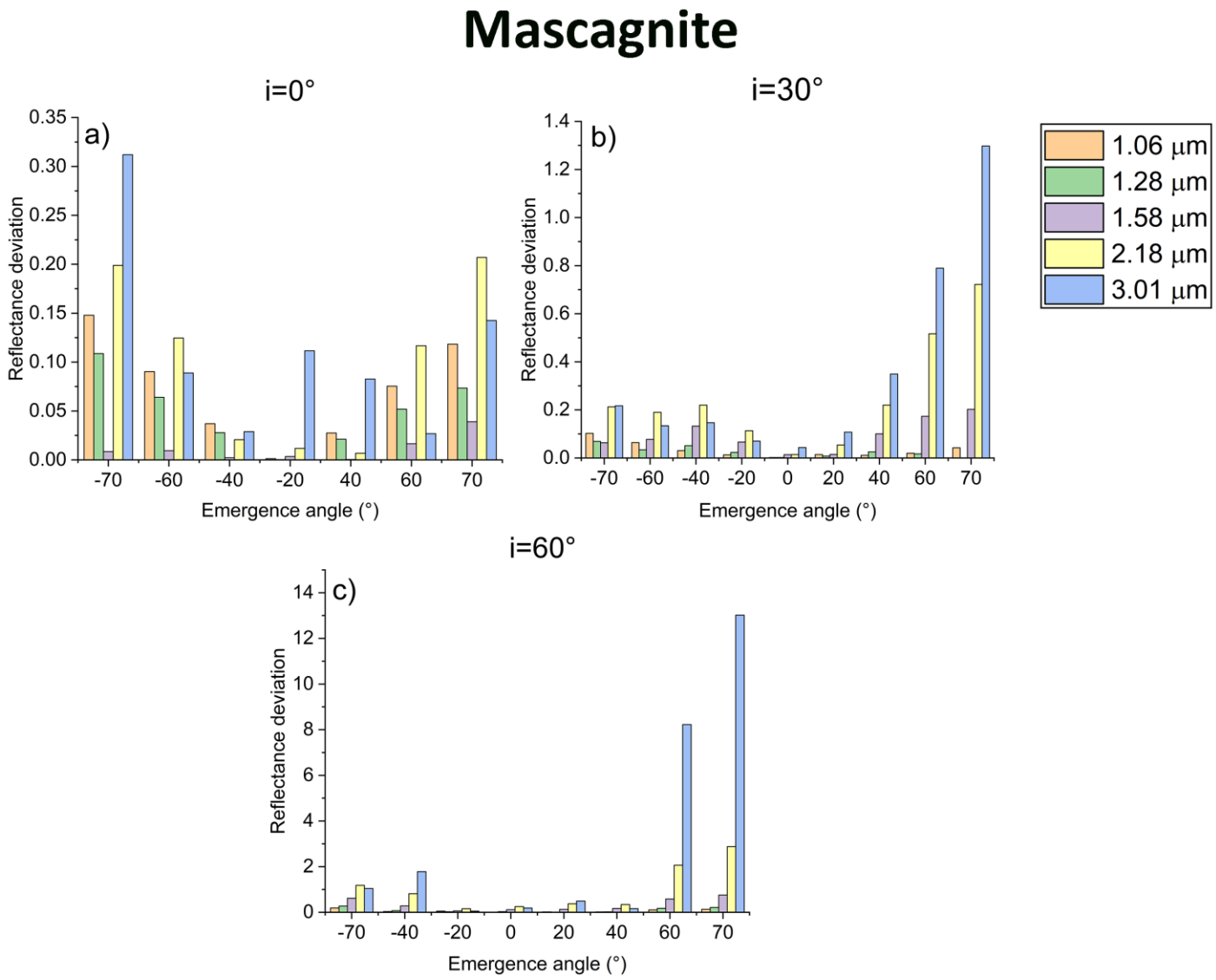

Fig. 15: *Histogram reports the deviation ratio relative to the spectrum collected with* reference *geometry (i=0° and e=20°), for incidence angles equal to 0° (a); 30° (b) and 60° (c) and emergence angles in the ± 70° range for the mascagnite sample. Note the different scales.*

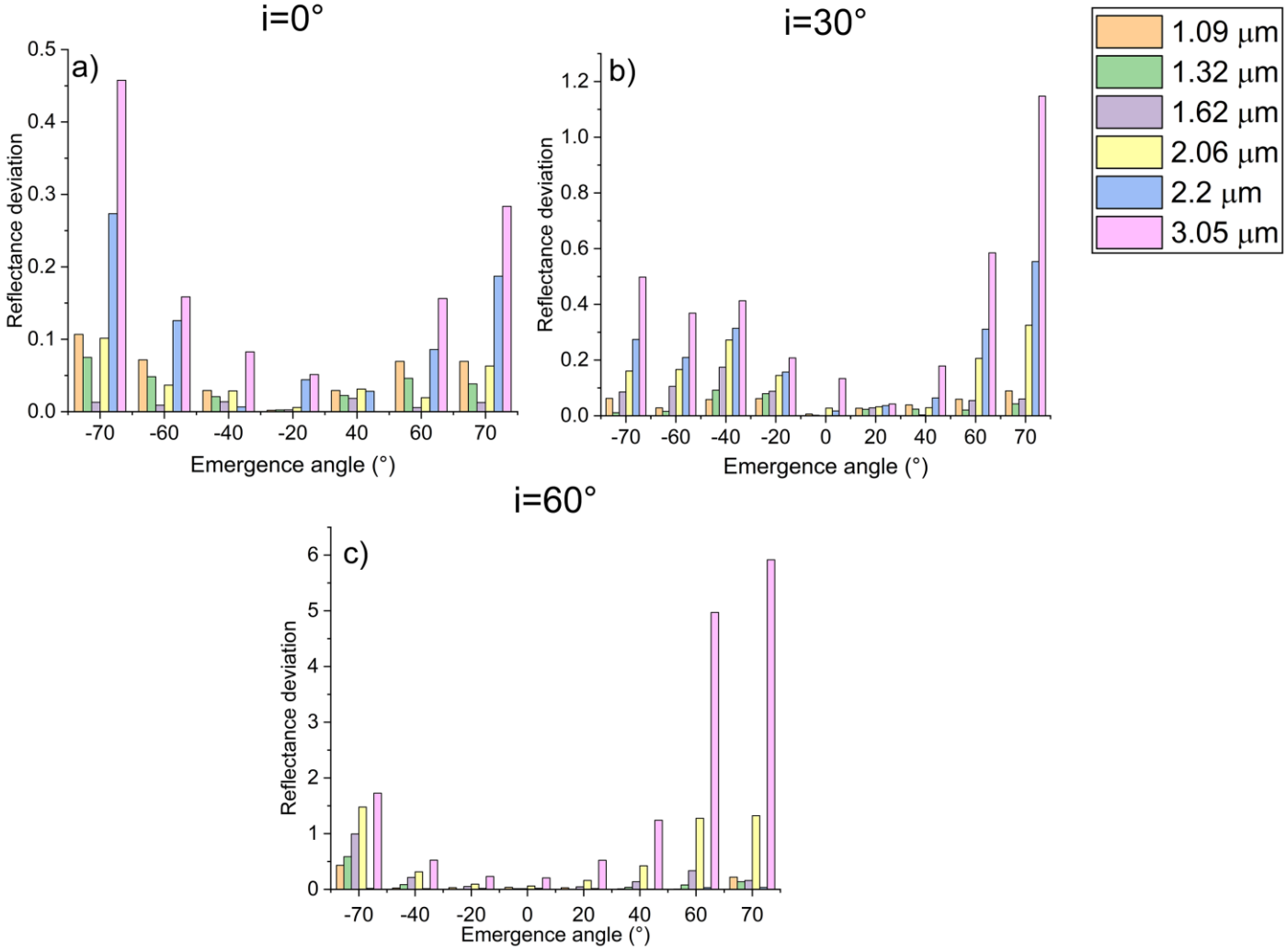

Fig.16: *Histogram reports the deviation ratio from relative to the spectrum collected with* reference *geometry (i=0° and e=20°), for incidence angles equal to 0° (a); 30° (b) and 60° (c) and emergence angles in the ± 70° range for the salammoniac sample. Note the different scales.*

In general, the relative change in reflectance values is already evident for small emergence angle variations (*e* = ± 20°). For *e* ≥40°, the spectral variation becomes significant and much more appreciable as shown in Figures 6 and 7. At geometric configurations with *i* = 60° and *e* ≥40° we can notice that the reflectance spectra of the inclined geometries tend to diverge from the one measured in nadir geometry.

Mascagnite sample displays a moderate monotonic increase of reflectance values, when varying the emergence angles for the NH_4^+ bands located at 1.06 and 1.28 µm with the highest values for *e* = -70°. The bands at 2.18 and 3.01 µm display an abrupt change when *e* ≥ 60°. These behaviours are the same for different incidence angles but much more marked for configurations with *i*= 60°. In fact, the 1.06 and 1.28 µm features with *i*=60° more drastically change their reflectance values (Figure 15). Salammoniac bands at 1.09 and 1.32 µm increase reflectance values reaching the highest ones for *e* ≥ 60° and *i* = 60°, whereas for *i* = 30° these two features do not show severe

changes (Figure 16). Regarding the bands above 2 µm, they are the most sensitive to variations in viewing geometries with a strong increase for $e \geq 40°$, especially also for $i = 60°$ (Figure 16).

The histograms in Figures 15 and 16 also show which geometric configurations and bands have the greatest variability. It is evident that the bands located at 1.58 and 1.62 µm, attributed to $2\nu_3$ NH_4^+ vibrational modes, are the less sensitive to changes in geometry. Furthermore, when increasing the incidence angle, the deviation drastically increases (Figure 15 and 16 c). The change in observation geometry affects all the selected features, in particular the bands located at 2.18 ($\nu_3 + \nu_4$) and 3.01 (ν_3) µm for mascagnite and 2.06 ($\nu_2 + \nu_3$), 2.2 ($\nu_3 + \nu_4$) and 3.05 (ν_3) µm for salammoniac. Finally, high incidence and negative emergence angles (forward scattering quadrant) have the highest reflectance deviation compared to positive equivalents (backward scattering quadrant) due to the shallow penetration depth of the light in the forward grazing geometries. The highest deviation is confirmed for incidence angles ≥ 30° and emergence angles ≥ 60°.

The results obtained in this work show that observation geometry can have a strong impact on band parameters, such as depth and area, in both ammonium-bearing minerals, in terms of shape of NH_4^+ absoption features. Incidence and emergence angles changes affect absorption bands and spectral slope. The different geometry configurations variously affect the continuum and absorption bands, especially for high incidence and emergence angles.

Although in literature (Beck et al., 2012, 2011) the variation in observation geometry is followed by a decrease in depth at larger phase angles, we notice a different trend related to the variations in both emergence and incidence angles. Considering angles of incidence close to nadir (0° and 30°), a twofold trend can be observed as the angle of emergence changes. An initial increase in area and depth values for small emergence angles up to about 20° and then its gradual decreases, especially for bands located above 2 µm. On the other hand, for $i = 60°$, we notice that for bands located at ~1.05, ~1.3, ~1.56 µm, depth and area generally decrease while the features at ~2.02, ~2.2 and ~3.0 µm have an opposite trend. This difference in behaviour between weak-medium bands and strong-to-nearly saturated bands is linked to the fact that at high incidence and phase angles the light penetrates to a shallower depth than for near normal incidence and consequently escapes with less absorption (smaller path through the medium). For the weak-medium bands it will thus increase their reflectance at band centre but to a smaller extent the continuum wavelengths around the band which are already weakly absorbing and have high reflectance. This effect reduces the depth and area of these bands with increasing phase angle. For strong-to-nearly saturated bands the reverse occurs. The continuum wavelengths around the band, which have medium reflectance levels, will significantly decrease their absorption and increase their reflectance, while the almost saturated band centres see only a moderate increase of their reflectance. Consequently, the band contrast ('relative' band depth and area) strongly increases when approaching grazing geometries. This interpretation is thus linked both to the non-linear radiative transfer in particulate media and to the way the individual band depth and area are defined, i.e. relative to their nearby reflectance maxima, called 'continuum', which have the tendency to have lower reflectance for strong bands than for weaker ones.

Finally, to summarise the behaviour of the band area and depth parameters, we calculated the relative percentage change from the reference observation configuration i=0° and e=20°. In order to provide a semi-quantitative relative percentage variation, we used the following normalisation:

505 $[(\Delta_e - \Delta_{emin})/(\Delta_{emax}-\Delta_{emin})]*100$

506 where,

507 - $\Delta_e = X_0 - X_e$, meaning X_0 the value of band parameters, either area or depth, at reference
508 observation configuration (i=0° and e=20°) and X_e the value of band parameters at each
509 emergence angle in the ±70° range.
510 - Δ_{emax}, meaning the maximum values of Δ_e in the studied dataset.
511 - Δ_{emin}, meaning the minimum values of Δ_e in the studied dataset.

512 This calculation was made for each absorption band analysed in this work. The results obtained
513 show that the relative percentage change in area and depth, considering the angle of incidence i=0,
514 varies from ~10% (e=- 20°) to ~37% (e= ±70°). Variations are significant at angles of incidence equal
515 to 60° and emergence ±70° with an average variation of ~70%. Both mascagnite and salammoniac
516 samples display single values of band area and depth percentage change of ~90% for i=0° and e=-
517 70°. The main difference between the two samples, in terms of relative percentage change, was
518 found for the i=0° configuration. In the mascagnite samples the percent variation is greater (from
519 ~20% at e= -20 to ~55% at e = 70°) than salammoniac (from ~5% at e= -20 to ~20% at e = 0°).

520 Our results indicate that variations of incidence and emergence angles generate changes in band
521 parameters and reflectance values with a band strength change non directly related to the
522 abundance of the presumed mineralogical phase. This supports the relevance of measuring the
523 BRDF of minerals and BRDF surfaces over wide wavelength ranges, both in the laboratory and for
524 the surfaces of Solar System objects.

525 *4.2 Implications for icy bodies*

526 The surface absorption feature of Ceres at 2.21 µm, in the remotly collected reflectance spectra,
527 has been attributed to the presence of NH_4^+, in good agreement with absorption characteristics of
528 the NH_4Cl mineral (De Sanctis et al., 2016). As reported in the present work, the 2.21 µm spectral
529 feature has a great variability in terms of depth and area under different viewing configurations,
530 thus implying that the band parameters variations in the Ceres's spectra may be due to different
531 observation geometries during the mapping of the surface by the *Dawn* mission (Russell and
532 Raymond, 2012) and not only in relation to the abundance of the NH_4Cl mineral. In analogy to the
533 previous spectral features, the band at ~3.05 µm for the salammoniac sample is also relevant,
534 relatively to its variations, for the detection of NH_4^+. In fact, the shape of the 3.05 µm band varies
535 under different viewing configurations, becoming more defined at high incidence angles compared
536 to other studies on ammonium minerals that describe the 3.05 µm feature as a broad water-
537 saturated band (e.g. Ehlmann et al., 2018; Ferrari et al., 2019).

538 Ammonium sulphate exhibits absorption characteristics located in the 3.0 – 3.3 µm spectral range,
539 consistent with the spectra of comet 67P as mapped by the Visible and InfraRed Thermal Imaging
540 Spectrometer, Mapping Channel (VIRTIS-M) instrument (Coradini et al., 2007). Poch et al. (2020)
541 propose the presence of ammonium salts (possibly including ammonium sulfate), mixed with
542 opaques, based on the well defined absoption bands at 3.1 and 3.3 µm. From the data we report in
543 the mascagnite sample, this specific spectral feature, has a great variability especially for high
544 incidence and emergence angles which may affect its correct identification and quantification from
545 remote observations.

In the *Virgil Fossae* area, on Pluto, two possible ammonia bands at ~1.65 and 2.21 μm were identified (Dalle Ore et al., 2019) by the Linear Etalon Imaging Spectral Array (LEISA) onboard the *New Horizons* mission (Schmitt et al., 2017). The 1.65 and 2.21 μm bands have been unambiguously attributed, similarly to the findings for Ceres, to the possible presence of ammonium minerals such as NH_4Cl related to recent cryovolcanism activity (Cruikshank et al., 2019). Furthermore, the surface of Charon, the largest Pluto's moon, shows the same absorption characteristics at 2.21 μm, attributed to hypothetical different ammonium minerals, in a non-univocal way given the similarity of the 2.21 μm band with that of ice. (Cook et al., 2018, 2007). The spectra here reported shown a great variability of the 2.21 μm features, related to the different viewing geometries especially at high emergence angle. The data collected in this work can help to understand if the NH_3 spectral feature on these bodies is either related to ammoniated salts, in this case salammoniac or mascagnite, or to other possible forms such as ice or other compounds. Recently, some features in the Charon's spectrum at 1.60 and 1.63 μm were dicovered for the first time, consistent with NH_4Cl absorption bands. Our data might provide information on its abundance on this moon (Cook et al., 2023). Finally, the data presented in this paper can be usefull to interpret the spectra from the Near-Infrared Spectrograph (NIRSpec) (Rauscher et al., 2007) on board the James Webb Space Telescope (JWST) of Trans Neptunian Object (TNO).

5. Conclusions

This study reported a systematic investigation of reflectance spectra in the near and visible infrared (1-4.2 μm) varying the observation geometries of two natural analogues ammonium bearing minerals, mascagnite [$(NH_4)_2SO_4$)] and salammoniac (NH_4Cl), with 32-80 μm powder granulometry and at room temperature. These data are of potentially great interest for the detection of nitrogen and ammonium compounds on the surface of icy objects. We analysed the effects of incidence and emergence angles, with a series of three different angles of incidence (i= 0°, 30° and 60°) and nine emergence angles in the range e= ±70°, on the spectral characteristics of NH_4^+ absorption features in order to provide laboratory data in relevant conditions to identify and quantify these minerals by remote sensing analysis.

We have shown that the collected reflectance spectra are affected by the change in observation geometries. We notice that divergence from nadir-like measurements becomes significant for e ≥40°. Characteristic NH_4^+ features are located at ~1.06, 1.3, 1.56, 2.02, 2.2 and 3.0 μm. Depth and area parameters of these features display a dual behaviour: (*i*) for absorption bands located below 2 μm and for incidence angles close to the azimuth and low emergence angles, the parameter values tend to increase, conversely, for high emergence angles, the values tend to decrease; (*ii*) spectral features above 2 μm generally increase with different trends depending on the angle of incidence. The greatest increase occurs for i = 60°. Reflectance values generally increase with increasing angle of incidence and angle of emission with maximum values for i = 60° and e = ±70° i.e. high phase angles and very low phase angles (opposition effect). However, bands below two microns reduce reflectance values increasing phase angles (g) especially for incidence angles equal to 0° and 30°.

The spectral features at ~3.0 μm show the clearest variation in shape resulting in its desaturation and corresponding better definition as geometry changes, important for remote sensing identification of NH_4^+ features.

Our results can have a direct aplication for differents objects inside the Solar System, especially small icy bodies. On these bodies, large surface slopes and surfaces characterised by rough topography are observed. The high emergence and incidence angles encountered during a probe fly-by can produce a misinterpretation when using laboratory spectra measured with nadir viewing geometries.

The use of laboratory data are needed to correctly deconvolve remote sensing hyperspectral data of planetary surfaces. The analysis of the surfaces of icy bodies for traces of NH_4^+ by current and future missions will provide important knowledge about the abundance of nitrogen on these bodies, their environment and their potential for the evolution of life. The laboratory spectra reported here add information on the band dependance on viewing geometries of two selected ammonium bearing minerals and should aid the remote data interpretation from *New Horizons*/LEISA and *Dawn*/VIR spectrometers.

Acknowledgments

This work has been done in the frame of the Trans-National Access program, project number 20-EPN2-081, of Europlanet 2024 RI which has received funding from the European Union's Horizon 2020 research and innovation program under grant agreement No 871149. We would like to thank the two anonymous reviewers for their suggestions and comments that greatly improved the manuscript.

On-line data

The complete sets of data (Fastelli et al. 2021b) presented in this paper are available online in the CSS database of the SSHADE database infrastructure (https://vwww.sshade.eu) [doi: 10.26302/SSHADE/EXPERIMENT_BS_20231304_001]

References

Beck, P., Barrat, J.-A., Grisolle, F., Quirico, E., Schmitt, B., Moynier, F., Gillet, P., Beck, C., 2011. NIR spectral trends of HED meteorites: Can we discriminate between the magmatic evolution, mechanical mixing and observation geometry effects? Icarus 216, 560–571. https://doi.org/10.1016/j.icarus.2011.09.015

Beck, P., Pommerol, A., Thomas, N., Schmitt, B., Moynier, F., Barrat, J.-A., 2012. Photometry of meteorites. Icarus 218, 364–377. https://doi.org/10.1016/j.icarus.2011.12.005

Berg, B.L., Cloutis, E.A., Beck, P., Vernazza, P., Bishop, J.L., Takir, D., Reddy, V., Applin, D., Mann, P., 2016. Reflectance spectroscopy (0.35–8μm) of ammonium-bearing minerals and qualitative comparison to Ceres-like asteroids. Icarus 265, 218–237. https://doi.org/10.1016/j.icarus.2015.10.028

Binzel, R.P., DeMeo, F.E., Burt, B.J., Cloutis, E.A., Rozitis, B., Burbine, T.H., Campins, H., Clark, B.E., Emery, J.P., Hergenrother, C.W., Howell, E.S., Lauretta, D.S., Nolan, M.C., Mansfield, M., Pietrasz, V., Polishook, D., Scheeres, D.J., 2015. Spectral slope variations for OSIRIS-REx target Asteroid (101955) Bennu: Possible evidence for a fine-grained regolith equatorial ridge. Icarus 256, 22–29. https://doi.org/10.1016/j.icarus.2015.04.011

Bishop, J.L., Bell III, J.F., Bell, J., Moersch, J.E., 2019. Remote Compositional Analysis: Techniques for Understanding Spectroscopy, Mineralogy, and Geochemistry of Planetary Surfaces. Cambridge University Press.

Bonnefoy, N., 2001. Développement d'un spectrophoto-goniomètre pour l'étude de la réflectance bidirectionnelle de surfaces géophysiques: application au soufre et perspectives pour le satellite Io. Grenoble 1.

Brissaud, O., Schmitt, B., Bonnefoy, N., Doute, S., Rabou, P., Grundy, W., Fily, M., 2004. Spectrogonio radiometer for the study of the bidirectional reflectance and polarization functions of planetary surfaces. 1. Design and tests. Applied optics 43, 1926–1937.

Ciarniello, M., De Angelis, S., Carli, C., De Sanctis, M.C., 2017. Photometric properties of Occator's bright spots analogue materials, in: European Planetary Science Congress. pp. EPSC2017-766.

Clark, B.E., Helfenstein, P., Bell, J.F., Peterson, C., Veverka, J., Izenberg, N.I., Domingue, D., Wellnitz, D., McFadden, L., 2002. NEAR Infrared Spectrometer Photometry of Asteroid 433 Eros. Icarus 155, 189–204. https://doi.org/10.1006/icar.2001.6748

Clark, R.N., Roush, T.L., 1984. Reflectance spectroscopy: Quantitative analysis techniques for remote sensing applications. Journal of Geophysical Research: Solid Earth 89, 6329–6340.

Comodi, P., Fastelli, M., Maturilli, A., Balic-Zunic, T., Zucchini, A., 2021. Emissivity and reflectance spectra at different temperatures of hydrated and anhydrous sulphates: A contribution to investigate the composition and dynamic of icy planetary bodies. Icarus 355, 114132.

Comodi, P., Mellini, M., Zanazzi, P.F., 1990. Scapolites; variation of structure with pressure and possible role in the storage of fluids. European Journal of Mineralogy 2, 195–202.

Comodi, P., Stagno, V., Zucchini, A., Fei, Y., Prakapenka, V., 2017. The compression behavior of blödite at low and high temperature up to∼ 10 GPa: Implications for the stability of hydrous sulfates on icy planetary bodies. Icarus 285, 137–144.

Cook, J.C., Dalle Ore, C.M., Protopapa, S., Binzel, R.P., Cartwright, R., Cruikshank, D.P., Earle, A., Grundy, W.M., Ennico, K., Howett, C., 2018. Composition of Pluto's small satellites: Analysis of New Horizons spectral images. Icarus 315, 30–45.

Cook, J.C., Desch, S.J., Roush, T.L., Trujillo, C.A., Geballe, T.R., 2007. Near-Infrared Spectroscopy of Charon: Possible Evidence for Cryovolcanism on Kuiper Belt Objects. ApJ 663, 1406–1419. https://doi.org/10.1086/518222

Cook, J.C., Protopapa, S., Dalle Ore, C.M., Cruikshank, D.P., Grundy, W.M., Lisse, C.M., Schmitt, B., Verbiscer, A., Singer, K.N., Spencer, J., Stern, S.A., Weaver, H.A., 2023. Analysis of Charon's spectrum at 2.21-μm from New Horizons/LEISA and Earth-based observations. Icarus 389, 115242. https://doi.org/10.1016/j.icarus.2022.115242

Coradini, A., Capaccioni, F., Drossart, P., Arnold, G., Ammannito, E., Angrilli, F., Barucci, A., Bellucci, G., Benkhoff, J., Bianchini, G., Bibring, J.P., Blecka, M., Bockelee-Morvan, D., Capria, M.T., Carlson, R., Carsenty, U., Cerroni, P., Colangeli, L., Combes, M., Combi, M., Crovisier, J., Desanctis, M.C.,

662 Encrenaz, E.T., Erard, S., Federico, C., Filacchione, G., Fink, U., Fonti, S., Formisano, V., Ip, W.H.,
663 Jaumann, R., Kuehrt, E., Langevin, Y., Magni, G., Mccord, T., Mennella, V., Mottola, S., Neukum, G.,
664 Palumbo, P., Piccioni, G., Rauer, H., Saggin, B., Schmitt, B., Tiphene, D., Tozzi, G., 2007. Virtis: An
665 Imaging Spectrometer for the Rosetta Mission. Space Sci Rev 128, 529–559.
666 https://doi.org/10.1007/s11214-006-9127-5
667 Cord, A.M., Pinet, P.C., Daydou, Y., Chevrel, S.D., 2003. Planetary regolith surface analogs:: optimized
668 determination of Hapke parameters using multi-angular spectro-imaging laboratory data. Icarus
669 165, 414–427.
670 Cruikshank, D.P., Grundy, W.M., DeMeo, F.E., Buie, M.W., Binzel, R.P., Jennings, D.E., Olkin, C.B., Parker,
671 J.W., Reuter, D.C., Spencer, J.R., Stern, S.A., Young, L.A., Weaver, H.A., 2015. The surface
672 compositions of Pluto and Charon. Icarus, Special Issue: The Pluto System 246, 82–92.
673 https://doi.org/10.1016/j.icarus.2014.05.023
674 Cruikshank, D.P., Umurhan, O.M., Beyer, R.A., Schmitt, B., Keane, J.T., Runyon, K.D., Atri, D., White, O.L.,
675 Matsuyama, I., Moore, J.M., McKinnon, W.B., Sandford, S.A., Singer, K.N., Grundy, W.M., Dalle Ore,
676 C.M., Cook, J.C., Bertrand, T., Stern, S.A., Olkin, C.B., Weaver, H.A., Young, L.A., Spencer, J.R., Lisse,
677 C.M., Binzel, R.P., Earle, A.M., Robbins, S.J., Gladstone, G.R., Cartwright, R.J., Ennico, K., 2019.
678 Recent cryovolcanism in Virgil Fossae on Pluto. Icarus 330, 155–168.
679 https://doi.org/10.1016/j.icarus.2019.04.023
680 Dalle Ore, C.M., Cruikshank, D.P., Protopapa, S., Scipioni, F., McKinnon, W.B., Cook, J.C., Grundy, W.M.,
681 Schmitt, B., Stern, S.A., Moore, J.M., 2019. Detection of ammonia on Pluto's surface in a region of
682 geologically recent tectonism. Science advances 5, eaav5731.
683 De Angelis, S., Carli, C., Tosi, F., Beck, P., Brissaud, O., Schmitt, B., Potin, S., De Sanctis, M.C., Capaccioni, F.,
684 Piccioni, G., 2019. NIR reflectance spectroscopy of hydrated and anhydrous sodium carbonates at
685 different temperatures. Icarus 317, 388–411. https://doi.org/10.1016/j.icarus.2018.08.012
686 De Angelis, S., De Sanctis, M.C., Ammannito, E., Carli, C., Di Iorio, T., Altieri, F., 2014. The Ma_Miss
687 instrument performance, I: Analysis of rocks powders by Martian VNIR spectrometer. Planetary and
688 Space Science 101, 89–107. https://doi.org/10.1016/j.pss.2014.06.010
689 De Angelis, S., Ferrari, M., De Sanctis, M.C., Ammannito, E., Raponi, A., Ciarniello, M., 2021a. High-
690 Temperature VIS-IR Spectroscopy of NH4-Phyllosilicates. Journal of Geophysical Research: Planets
691 126, e2020JE006696.
692 De Angelis, S., Tosi, F., Carli, C., Potin, S., Beck, P., Brissaud, O., Schmitt, B., Piccioni, G., De Sanctis, M.C.,
693 Capaccioni, F., 2021b. Temperature-dependent, VIS-NIR reflectance spectroscopy of sodium
694 sulfates. Icarus 357, 114165.
695 De Sanctis, M.C., Raponi, A., Ammannito, E., Ciarniello, M., Toplis, M.J., McSween, H.Y., Castillo-Rogez, J.C.,
696 Ehlmann, B.L., Carrozzo, F.G., Marchi, S., Tosi, F., Zambon, F., Capaccioni, F., Capria, M.T., Fonte, S.,
697 Formisano, M., Frigeri, A., Giardino, M., Longobardo, A., Magni, G., Palomba, E., McFadden, L.A.,
698 Pieters, C.M., Jaumann, R., Schenk, P., Mugnuolo, R., Raymond, C.A., Russell, C.T., 2016. Bright
699 carbonate deposits as evidence of aqueous alteration on (1) Ceres. Nature 536, 54–57.
700 https://doi.org/10.1038/nature18290
701 De Sanctis, M.C., Mitri, G., Castillo-Rogez, J., House, C.H., Marchi, S., Raymond, C.A., Sekine, Y., 2020. Relict
702 Ocean Worlds: Ceres. Space Sci Rev 216, 60. https://doi.org/10.1007/s11214-020-00683-w
703 Ehlmann, B.L., Hodyss, R., Bristow, T.F., Rossman, G.R., Ammannito, E., De Sanctis, M.C., Raymond, C.A.,
704 2018. Ambient and cold-temperature infrared spectra and XRD patterns of ammoniated
705 phyllosilicates and carbonaceous chondrite meteorites relevant to Ceres and other solar system
706 bodies. Meteoritics & Planetary Science 53, 1884–1901. https://doi.org/10.1111/maps.13103
707 Fastelli, M., Comodi, P., Maturilli, A., Zucchini, A., 2020. Reflectance Spectroscopy of Ammonium Salts:
708 Implications for Planetary Surface Composition. Minerals 10, 902.
709 https://doi.org/10.3390/min10100902
710 Fastelli, M., Comodi, P., Schmitt, B., Beck, P., Poch, O., Sassi, P., Zucchini, A., 2022. Reflectance spectra (1–5
711 μm) at low temperatures and different grain sizes of ammonium-bearing minerals relevant for icy
712 bodies. Icarus 115055.

713 Fastelli, M., Zucchini, A., Comodi, P., Maturilli, A., Alemanno, G., Palomba, E., Piergallini, R., 2021. NIR-MID
714 Reflectance and Emissivity Study at Different Temperatures of Sodium Carbonate Minerals: Spectra
715 Characterization and Implication for Remote Sensing Identification. Minerals 11, 845.
716 Fastelli, M., Schmitt, B., Beck, P., Poch, O., Comodi, P., 2021b. Near-infrared BRDF spectra in the principal
717 plane of Salammoniac and Mascagnite 32-80µm grain size powders at 300K. SSHADE/CSS (OSUG
718 Data Center). Dataset/Spectral Data. doi: 10.26302/SSHADE/EXPERIMENT_BS_20231304_001
719 Ferrari, M., De Angelis, S., De Sanctis, M.C., Ammannito, E., Stefani, S., Piccioni, G., 2019. Reflectance
720 spectroscopy of ammonium-bearing phyllosilicates. Icarus 321, 522–530.
721 https://doi.org/10.1016/j.icarus.2018.11.031
722 Fornasier, S., Hasselmann, P.H., Barucci, M.A., Feller, C., Besse, S., Leyrat, C., Lara, L., Gutierrez, P.J., Oklay,
723 N., Tubiana, C., Scholten, F., Sierks, H., Barbieri, C., Lamy, P.L., Rodrigo, R., Koschny, D., Rickman, H.,
724 Keller, H.U., Agarwal, J., A'Hearn, M.F., Bertaux, J.-L., Bertini, I., Cremonese, G., Deppo, V.D.,
725 Davidsson, B., Debei, S., Cecco, M.D., Fulle, M., Groussin, O., Güttler, C., Hviid, S.F., Ip, W., Jorda, L.,
726 Knollenberg, J., Kovacs, G., Kramm, R., Kührt, E., Küppers, M., Forgia, F.L., Lazzarin, M., Moreno,
727 J.J.L., Marzari, F., Matz, K.-D., Michalik, H., Moreno, F., Mottola, S., Naletto, G., Pajola, M.,
728 Pommerol, A., Preusker, F., Shi, X., Snodgrass, C., Thomas, N., Vincent, J.-B., 2015.
729 Spectrophotometric properties of the nucleus of comet 67P/Churyumov-Gerasimenko from the
730 OSIRIS instrument onboard the ROSETTA spacecraft. A&A 583, A30. https://doi.org/10.1051/0004-
731 6361/201525901
732 Fortes, A.D., Choukroun, M., 2010. Phase Behaviour of Ices and Hydrates. Space Sci Rev 153, 185–218.
733 https://doi.org/10.1007/s11214-010-9633-3
734 Fortes, A.D., Grindrod, P.M., Trickett, S.K., Vočadlo, L., 2007. Ammonium sulfate on Titan: Possible origin
735 and role in cryovolcanism. Icarus 188, 139–153. https://doi.org/10.1016/j.icarus.2006.11.002
736 Füri, E., Marty, B., 2015. Nitrogen isotope variations in the Solar System. Nature Geoscience 8, 515–522.
737 Gatta, G.D., Comodi, P., Zanazzi, P.F., Ballaran, T.B., 2005. Anomalous elastic behavior and high-pressure
738 structural evolution of zeolite levyne. American Mineralogist 90, 645–652.
739 Guidobaldi, G., Cambi, C., Cecconi, M., Comodi, P., Deneele, D., Paris, M., Russo, G., Vitale, E., Zucchini, A.,
740 2018. Chemo-mineralogical evolution and microstructural modifications of a lime treated
741 pyroclastic soil. Engineering Geology 245, 333–343. https://doi.org/10.1016/j.enggeo.2018.09.012
742 Hapke, B., 2012. Theory of reflectance and emittance spectroscopy. Cambridge university press.
743 Hapke, B., 1986. Bidirectional reflectance spectroscopy: 4. The extinction coefficient and the opposition
744 effect. Icarus 67, 264–280. https://doi.org/10.1016/0019-1035(86)90108-9
745 Hapke, B., 1981. Bidirectional reflectance spectroscopy: 1. Theory. Journal of Geophysical Research: Solid
746 Earth 86, 3039–3054.
747 Hasebe, K., 1981. Studies of the crystal structure of ammonium sulfate in connection with its ferroelectric
748 phase transition. Journal of the Physical Society of Japan 50, 1266–1274.
749 Kargel, J.S., 1992. Ammonia-water volcanism on icy satellites: Phase relations at 1 atmosphere. Icarus 100,
750 556–574. https://doi.org/10.1016/0019-1035(92)90118-Q
751 King, T.V., Clark, R.N., Calvin, W.M., Sherman, D.M., Brown, R.H., 1992. Evidence for ammonium-bearing
752 minerals on Ceres. Science 255, 1551–1553.
753 Krohn, M.D., Altaner, S.P., 1987. Near-infrared detection of ammonium minerals. GEOPHYSICS 52, 924–930.
754 https://doi.org/10.1190/1.1442362
755 Larson, A.C., Von Dreele, R.B., 1987. Generalized structure analysis system (GSAS). Los Alamos National
756 Laboratory LA-UR-86-748.
757 Levy, H.A., Peterson, S.W., 1952. Neutron diffraction study of the crystal structure of ammonium chloride.
758 Physical Review 86, 766.
759 Magrin, S., La Forgia, F., Pajola, M., Lazzarin, M., Massironi, M., Ferri, F., Da Deppo, V., Barbieri, C., Sierks,
760 H., 2012. (21) Lutetia spectrophotometry from Rosetta-OSIRIS images and comparison to ground-
761 based observations. Planetary and Space Science, Rosetta Fly-by at Asteroid (21) Lutetia 66, 43–53.
762 https://doi.org/10.1016/j.pss.2011.10.001

763 Mustard, J.F., Glotch, T.D., 2019. Theory of Reflectance and Emittance Spectroscopy of Geologic Materials
764 in the Visible and Infrared Regions. Remote Compositional Analysis: Techniques for Understanding
765 Spectroscopy, Mineralogy, and Geochemistry of Planetary Surfaces 21–41.
766 Neish, C.D., Prockter, L.M., Patterson, G.W., 2012. Observational constraints on the identification and
767 distribution of chaotic terrain on icy satellites. Icarus 221, 72–79.
768 https://doi.org/10.1016/j.icarus.2012.07.009
769 Nelson, R.M., Buratti, B.J., Wallis, B.D., Lane, A.L., West, R.A., Simmons, K.E., Hord, C.W., Esposito, L.W.,
770 1987. Voyager 2 Photopolarimeter observations of the Uranian satellites. Journal of Geophysical
771 Research: Space Physics 92, 14905–14910. https://doi.org/10.1029/JA092iA13p14905
772 Pelkey, S.M., Mustard, J.F., Murchie, S., Clancy, R.T., Wolff, M., Smith, M., Milliken, R., Bibring, J.-P.,
773 Gendrin, A., Poulet, F., Langevin, Y., Gondet, B., 2007. CRISM multispectral summary products:
774 Parameterizing mineral diversity on Mars from reflectance. Journal of Geophysical Research:
775 Planets 112. https://doi.org/10.1029/2006JE002831
776 Pilorget, C., Okada, T., Hamm, V., Brunetto, R., Yada, T., Loizeau, D., Riu, L., Usui, T., Moussi-Soffys, A.,
777 Hatakeda, K., Nakato, A., Yogata, K., Abe, M., Aléon-Toppani, A., Carter, J., Chaigneau, M., Crane, B.,
778 Gondet, B., Kumagai, K., Langevin, Y., Lantz, C., Le Pivert-Jolivet, T., Lequertier, G., Lourit, L.,
779 Miyazaki, A., Nishimura, M., Poulet, F., Arakawa, M., Hirata, N., Kitazato, K., Nakazawa, S., Namiki,
780 N., Saiki, T., Sugita, S., Tachibana, S., Tanaka, S., Yoshikawa, M., Tsuda, Y., Watanabe, S., Bibring, J.-
781 P., 2022. First compositional analysis of Ryugu samples by the MicrOmega hyperspectral
782 microscope. Nat Astron 6, 221–225. https://doi.org/10.1038/s41550-021-01549-z
783 Pisello, A., De Angelis, S., Ferrari, M., Porreca, M., Vetere, F.P., Behrens, H., De Sanctis, M.C., Perugini, D.,
784 2022a. Visible and near-InfraRed (VNIR) reflectance of silicate glasses: Characterization of a
785 featureless spectrum and implications for planetary geology. Icarus 374, 114801.
786 https://doi.org/10.1016/j.icarus.2021.114801
787 Pisello, A., Ferrari, M., De Angelis, S., Vetere, F.P., Porreca, M., Stefani, S., Perugini, D., 2022b. Reflectance
788 of silicate glasses in the mid-infrared region (MIR): Implications for planetary research. Icarus 388,
789 115222.
790 Poch, O., Istiqomah, I., Quirico, E., Beck, P., Schmitt, B., Theulé, P., Faure, A., Hily-Blant, P., Bonal, L., Raponi,
791 A., Ciarniello, M., Rousseau, B., Potin, S., Brissaud, O., Flandinet, L., Filacchione, G., Pommerol, A.,
792 Thomas, N., Kappel, D., Mennella, V., Moroz, L., Vinogradoff, V., Arnold, G., Erard, S., Bockelée-
793 Morvan, D., Leyrat, C., Capaccioni, F., De Sanctis, M.C., Longobardo, A., Mancarella, F., Palomba, E.,
794 Tosi, F., 2020. Ammonium salts are a reservoir of nitrogen on a cometary nucleus and possibly on
795 some asteroids. Science 367, eaaw7462. https://doi.org/10.1126/science.aaw7462
796 Pommerol, A., Schmitt, B., 2008a. Strength of the H2O near-infrared absorption bands in hydrated
797 minerals: Effects of measurement geometry. Journal of Geophysical Research: Planets 113.
798 https://doi.org/10.1029/2008JE003197
799 Pommerol, A., Schmitt, B., 2008b. Strength of the H2O near-infrared absorption bands in hydrated
800 minerals: Effects of particle size and correlation with albedo. Journal of Geophysical Research:
801 Planets 113.
802 Potin, S., Beck, P., Schmitt, B., Moynier, F., 2019. Some things special about NEAs: Geometric and
803 environmental effects on the optical signatures of hydration. Icarus 333, 415–428.
804 Quinn, R.C., Chittenden, J.D., Kounaves, S.P., Hecht, M.H., 2011. The oxidation-reduction potential of
805 aqueous soil solutions at the Mars Phoenix landing site. Geophysical Research Letters 38.
806 https://doi.org/10.1029/2011GL047671
807 Rauscher, B.J., Fox, O., Ferruit, P., Hill, R.J., Waczynski, A., Wen, Y., Xia-Serafino, W., Mott, B., Alexander, D.,
808 Brambora, C.K., 2007. Detectors for the James Webb Space Telescope Near-Infrared Spectrograph.
809 I. Readout Mode, Noise Model, and Calibration Considerations. Publications of the Astronomical
810 Society of the Pacific 119, 768.
811 Rietveld, H.M., 1969. A profile refinement method for nuclear and magnetic structures. Journal of applied
812 Crystallography 2, 65–71.

Russell, C.T., Raymond, C.A., 2012. The Dawn Mission to Vesta and Ceres, in: Russell, C., Raymond, C. (Eds.), The Dawn Mission to Minor Planets 4 Vesta and 1 Ceres. Springer, New York, NY, pp. 3–23. https://doi.org/10.1007/978-1-4614-4903-4_2

Schmitt, B., Philippe, S., Grundy, W.M., Reuter, D.C., Côte, R., Quirico, E., Protopapa, S., Young, L.A., Binzel, R.P., Cook, J.C., Cruikshank, D.P., Dalle Ore, C.M., Earle, A.M., Ennico, K., Howett, C.J.A., Jennings, D.E., Linscott, I.R., Lunsford, A.W., Olkin, C.B., Parker, A.H., Parker, J.Wm., Singer, K.N., Spencer, J.R., Stansberry, J.A., Stern, S.A., Tsang, C.C.C., Verbiscer, A.J., Weaver, H.A., 2017. Physical state and distribution of materials at the surface of Pluto from New Horizons LEISA imaging spectrometer. Icarus, Special Issue: The Pluto System 287, 229–260. https://doi.org/10.1016/j.icarus.2016.12.025

Schröder, S.E., Grynko, Ye., Pommerol, A., Keller, H.U., Thomas, N., Roush, T.L., 2014. Laboratory observations and simulations of phase reddening. Icarus 239, 201–216. https://doi.org/10.1016/j.icarus.2014.06.010

Sefton-Nash, E., Catling, D.C., Wood, S.E., Grindrod, P.M., Teanby, N.A., 2012. Topographic, spectral and thermal inertia analysis of interior layered deposits in Iani Chaos, Mars. Icarus 221, 20–42.

Singer, R.B., McCord, T.B., Clark, R.N., Adams, J.B., Huguenin, R.L., 1979. Mars surface composition from reflectance spectroscopy: A summary. Journal of Geophysical Research: Solid Earth 84, 8415–8426. https://doi.org/10.1029/JB084iB14p08415

Stephan, K., Jaumann, R., Krohn, K., Schmedemann, N., Zambon, F., Tosi, F., Carrozzo, F.G., McFadden, L.A., Otto, K., De Sanctis, M.C., Ammannito, E., Matz, K.-D., Roatsch, T., Preusker, F., Raymond, C.A., Russell, C.T., 2017. An investigation of the bluish material on Ceres. Geophysical Research Letters 44, 1660–1668. https://doi.org/10.1002/2016GL071652

Toby, B.H., 2001. EXPGUI, a graphical user interface for GSAS. Journal of applied crystallography 34, 210–213.

Wang, C.H., Wright, R.B., 1974. Raman scattering study of the effect of pressure and temperature on the order-disorder phase transition in ammonium chloride. The Journal of Chemical Physics 60, 849–854.

Warell, J., Bergfors, C., 2008. Mercury's integral phase curve: Phase reddening and wavelength dependence of photometric quantities. Planetary and Space Science 56, 1939–1948. https://doi.org/10.1016/j.pss.2008.09.002